aerospace

MDPI

Article

Adaptive Nonsingular Fast Terminal Sliding Mode Control for Space Robot Based on Wavelet Neural Network Under Lumped Uncertainties

Junwei Mei [1,†], Yawei Zheng [1,†], Haiping Ai [1,2,*], Feilong Xiong [1], An Zhu [1,*] and Xiaodong Fu [3]

[1] School of Energy and Mechanical Engineering, Jiangxi University of Science and Technology, Nanchang 330013, China; 5720230312@mail.jxust.edu.cn (J.M.); 6720231553@mail.jxust.edu.cn (Y.Z.); 9520070001@jxust.edu.cn (F.X.)
[2] School of Mechanical Engineering and Automation, Fuzhou University, Fuzhou 350108, China
[3] School of Aerospace Engineering, Tsinghua University, Beijing 100084, China; fuxiaodong@mail.tsinghua.edu.cn
* Correspondence: ahpwuhan@163.com (H.A.); 9520230011@jxust.edu.cn (A.Z.)
† These authors contributed equally to this work.

Abstract

This paper proposes an adaptive wavelet neural network nonsingular fast terminal sliding mode control strategy based on a finite-time framework for a space robot system under external disturbances and model uncertainties. Firstly, the dynamic model of space robot is established based on the second Lagrange equation. Unlike sliding mode control, which converges asymptotically, terminal sliding mode control (TSMC) has been proposed to ensure finite-time convergence for a space robot system. Based on the aforementioned TSMC framework, the fast terminal sliding mode control (FTSMC) is proposed to enhance system convergence rate. However, TSMC exhibits a singularity issue attributed to the presence of negative fractional order. To avoid this issue, a nonsingular fast terminal sliding mode controller (NFTSMC) has been proposed. The controller is designed to integrate linear and nonlinear terms into a novel nonsingular fast terminal sliding mode surface. The method achieves fast finite-time convergence concurrently with improved robustness, while effectively avoiding singularities. To compensate for external disturbances and model uncertainties in the space robot system, this paper proposes the combination of wavelet neural network (WNN) for the real-time estimation of lumped uncertainties. Network parameters are dynamically adjusted via an adaptive law to mitigate chattering effectively and enhance trajectory tracking precision. Utilizing Lyapunov stability theory and numerical simulations, the space robot system's stability is rigorously proven and the controller effectiveness is validated. Compared with the traditional NFTSMC, the proposed control strategy reduces the convergence time by 20.74%. In the case of trajectory tracking comparison, the root mean square error (RMSE) improves by 35.85%, the mean tracking error improves by 63.29%, the integral of absolute error (IAE) improves by 29.37%, and the integral of time-weighted absolute error (ITAE) improves by 93.06%. Additionally, a comparative simulation with RBFNN is included in this paper. Compared with RBFNN, the proposed control strategy reduces input torque energy consumption by 77.36% and improves control smoothness by 87.03%, quantitatively demonstrating the effectiveness of the proposed control strategy.

Keywords: nonsingular fast terminal sliding mode control strategy; model uncertainties; adaptive wavelet neural network; fast finite-time convergence; trajectory tracking

Check for updates

Academic Editor: Paolo Tortora

Received: 13 February 2026
Revised: 29 March 2026
Accepted: 29 March 2026
Published: 2 April 2026

Copyright: © 2026 by the authors. Licensee MDPI, Basel, Switzerland. This article is an open access article distributed under the terms and conditions of the Creative Commons Attribution (CC BY) license.

1. Introduction

Recent developments in robotic technology have made space robots increasingly popular; they have a wide range of applications in space exploration, which makes them critical tools for spacecraft performing various on-orbit tasks. This is especially true for crucial missions such as the maintenance and repair of space stations, servicing and upgrading of satellites, and removal of space debris. To ensure these tasks are completed safely and effectively, greater robustness and superior control performance are required of the space robots. However, unlike ground-based robots, the control design of space robots presents a set of complex challenges due to the specific outer environment and the complicated kinematic characteristics of the space robot system. This is because space robots operate in a microgravity environment that satisfies nonholonomic dynamic constraints. Consequently, the motion of the base and the linkages impact each other, resulting in a strongly coupled and highly nonlinear system [1]. Additionally, external disturbances, such as variations in the solar wind, can affect the stability of the space robot system. Furthermore, model uncertainties arising from biases in system parameter identification can further complicate the kinetics and negatively affect tracking performance. Therefore, significant challenges exist regarding the trajectory tracking problem for space robots with model uncertainties.

To satisfy the control requirements of space robots, researchers have developed a variety of nonlinear control methods, including fuzzy control [2,3], optimal control [4,5], model predictive control (MPC) [6,7], and sliding mode control (SMC). Of these methods, SMC is widely regarded as an effective strategy for handling nonlinear disturbed systems due to its notable characteristics, such as a fast response time, minimal overshoot and strong robustness to uncertainties and disturbances. In [8], the tracking performance and robustness of the system were enhanced by employing Linear Extended State Observer (LESO) based on adaptive SMC to estimate the lumped disturbance. Ref. [9] integrates SMC with continuous and periodic event-triggered approaches, effectively confining the sliding variables to a quasi-sliding mode and significantly enhancing control efficiency. Reference [10] presents a novel sliding surface design based on disturbance estimation. While this approach exhibits a simple structural design, it struggles to manage complex systems. Despite the strong robustness of SMC, conventional linear SMC leads to chattering phenomena and achieves only asymptotic convergence of system errors. To mitigate chattering and achieve finite-time convergence [11], researchers have developed the terminal sliding mode control (TSMC) strategy. TSMC possesses a fractional order term, as the error approaches zero, this term converges to zero, thereby achieving finite-time convergence. In the literature [12], an integrated sliding surface is designed, to achieve finite-time convergence while guaranteeing system robustness. Reference [13] developed a continuous TSMC strategy that achieves continuous control input while guaranteeing finite-time stability. However, it should be noted that this can negatively impact the convergence time. To enhance convergence speed, researchers have proposed fast terminal sliding mode control (FTSMC) strategy. Specifically, the global FTSMC method in Reference [14] guarantees finite-time convergence of all system state tracking errors to zero, encompassing both position and velocity variables. Ref. [15] utilizes an adaptive backstepping FTSMC approach to design a fast finite-time tracking controller. In contrast to traditional TSMC, the FTSMC strategy exhibits a superior convergence rate even under conditions of substantial initial state deviation from equilibrium.

However, the design of the sliding mode surface incorporates a nonlinear term with a negative fractional order, which approaches infinity when errors become infinitesimally small. This behavior gives rise to a singularity problem present in both TSMC and FTSMC methodology. To address this issue, ref. [16] proposed a nonsingular terminal sliding

mode control (NTSMC) scheme, which designs a novel sliding mode function and puts forward a reaching law to reach a sliding mode surface. The existence of a linear term and fractional nonlinear term in the sliding mode function facilitates finite-time convergence of the system and avoids the singularity issue. In [17], an adaptive disturbance observer is proposed to compensate the unknown disturbance within a fixed-time. This is combined with NTSMC to design a novel nonsingular terminal sliding mode surface, ensuring that the upper bound of the convergence time is independent of system initial states. Based on the NTSMC framework, ref. [18] introduces a NTSMC-RBFNN controller to compensate for multiple uncertainties. These studies demonstrate the wide range of application of NTSMC. Furthermore, to achieve accelerated convergence, an enhanced control strategy termed nonsingular fast terminal sliding mode control (NFTSMC) has been introduced, building upon NTSMC framework.

Due to their fast finite-time convergence characteristics, NFTSMC is becoming increasing popular in high-precision control applications across various engineering domains. In reference [19], a high-order integral NFTSMC is proposed, integrated with a perturbation estimation scheme, for a class of nonlinear systems exhibiting hysteresis. The controller ensures finite-time error convergence, thereby strengthening the system's robustness against disturbances and uncertainties. Another study [20] puts forward a high-order super-twisting observer (HOSTO) and a NFTSMC implementation, resulting in rapid convergence of trajectory tracking errors. To circumvent the singularity issue in TSMC and accelerate its convergence rate, NFTSMC was developed as described in [21] to achieve finite-time trajectory tracking. However, model uncertainties in the existing system can adversely affect tracking performance. Reference [22] proposes a NFTSMC strategy to mitigate the chattering issue inherent in conventional sliding mode control and circumvent the singularity problem associated with TSMC. Furthermore, it demonstrates faster convergence speeds than traditional NTSMC. Given these findings, a control framework based on NFTSMC is employed to achieve fast convergence in finite time. This framework is designed to ensure the system effectively inherits all the aforementioned advantages.

In complex space environments, external factors such as extreme temperatures and space radiation adversely affect the inertial parameters of space robot system. In the design of control system, these variations manifest as model uncertainties, consistently posing challenges to system stability and control accuracy. When a space robot is subjected to large-scale external disturbances, these uncertainties can degrade control performance and negatively impact system stability. Extensive research has been undertaken to compensate for the model uncertainties of space robot systems [23]. Neural networks (NN) have demonstrated effectiveness in estimating and compensating for these system uncertainties due to their powerful data processing capabilities. Researchers have found that the Radial Basis Function (RBF) neural network has a capability to approximate any nonlinear function with high precision. Therefore, the RBFNN has found widespread application in estimating the upper bounds of system uncertainties. In [24], a NTSMC is proposed, which achieves finite-time convergence. To mitigate disturbances from uncertainties, an RBF neural network was incorporated to reduce chattering simultaneously. Reference [25] aims to address the unknown disturbances and lumped uncertainties of the system by designing a fractional-order NTSMC methodology. Unlike RBF neural networks, wavelet neural network (WNN) possesses the time-frequency localization properties, making them a powerful approximation tool.

In recent years, researchers have shown a growing interest in using Wavelet Neural Networks to approximate the bounds of uncertainties. Reference [26] uses a functional linkage wavelet neural network (FLWNN) to approximate an ideal sliding mode controller. Estimating the output weights of the functional link structure improves the learning

abilities of system. Based on a fixed-time NFTSMC framework, reference [27] proposes an adaptive fuzzy wavelet neural network (AFWNN) algorithm, which effectively overcomes the negative effects of uncertainties in robotic manipulator systems. To achieve effective estimation of model parameters, reference [28] introduces a gradient descent-based B-spline WNN within an indirect adaptive control framework. The adaptation is realized through a recursive least squares algorithm, enabling the estimation of complex system uncertainties. Reference [29] presents a wavelet-based observer for real-time estimation of modeling errors, external disturbances, and uncertainties arising in dynamic surface control of jointed robots, thereby improving tracking precision. Reference [30] introduces an adaptive algorithm combining the basis function of a WNN with a fuzzy system to achieve accurate approximation of the plant model function. This approach effectively utilizes the time domain localization of wavelets and the reasoning power of fuzzy systems, resulting in improved plant model estimation. Furthermore, we combined a WNN by designing an adaptive law to adjust the parameters of controller in real-time, thereby reducing chattering caused by changes in the system gains.

Based on the previous discussion, developing a robust control scheme that guarantees fast finite-time convergence for a space robot system under external disturbances and model uncertainties caused by extreme temperature remains a substantial and open challenge. To overcome these problems, this paper develops a novel adaptive control strategy that integrates NFTSMC strategy with WNN for a space robot system. Using the finite-time framework, the NFTSMC strategy designs a novel sliding mode surface. This approach uses fractional order and linear terms to guarantee fast convergence speeds while avoiding singularity. Furthermore, to address model uncertainties arising from a complicated external environment, WNN is employed to approximate the supremum of lumped uncertainties. Leveraging its capability to handle large amounts of data and design an adaptive law to adjust the network parameters online, WNN can effectively improve the tracking accuracy of space robots. Ultimately, utilizing Lyapunov stability theory enables the rigorous demonstration of the feasibility of the proposed strategy. Moreover, comparative analysis validates the superiority of the proposed controller outperform conventional approaches, as measured by accelerated convergence, enhanced tracking precision, and improved robust stability.

The contributions of the paper are summarized below:

(1) To achieve fast finite-time convergence, a new NFTSMC is proposed. It avoids the singularity issue of TSMC while retaining the rapid convergence of FTMC.
(2) To mitigate chattering, a nonsingular fast terminal sliding mode surface is designed, along with a fast terminal sliding mode power reaching law that combines linear and nonlinear terms. The nonlinear term, characterized by a non-negative fractional order to ensure finite-time convergence, and the linear term enhance convergence rate, both of which significantly mitigate the system chattering and improve the robustness of the space robot system.
(3) To compensate for model uncertainties, a WNN is used to estimate their bounds. Mitigating disturbances from these uncertainties using the WNN significantly improves trajectory tracking accuracy.

This paper proceeds as follows: Section 2 introduces the derivation of the space robot dynamic model and a review of essential preliminaries. Section 3 describes the controller design. The stability of the closed-loop system under the proposed controller is rigorously proven in Section 4 through Lyapunov analysis, which in turn guarantees the control strategy's effectiveness. Section 5 presents the numerical simulation analyses. Section 6 is the conclusion of the article.

2. Model Formulation and Foundational Preliminaries

Dynamic Modeling

The space robot model, as illustrated in Figure 1, and the corresponding parameters are summarized in Section 5. According to [31], the system dynamic equation simplified representation is:

$$\boldsymbol{D}(\boldsymbol{q})\ddot{\boldsymbol{q}} + \boldsymbol{H}(\boldsymbol{q}, \dot{\boldsymbol{q}})\dot{\boldsymbol{q}} = \boldsymbol{\tau}(t) \tag{1}$$

where $\boldsymbol{q}$, $\dot{\boldsymbol{q}}$ and $\ddot{\boldsymbol{q}} \in \boldsymbol{R}^{n\times 1}$ denote the position, velocity, and acceleration vectors of the space robot system. $\boldsymbol{D}(\boldsymbol{q}) \in \boldsymbol{R}^{n\times n}$ represents the mass inertia matrix. $\boldsymbol{H}(\boldsymbol{q}, \dot{\boldsymbol{q}}) \in \boldsymbol{R}^{n\times n}$ represents the Coriolis and Centrifugal Matrix. Moreover, $\boldsymbol{\tau}(t)$ indicates the torque applied to the joint.

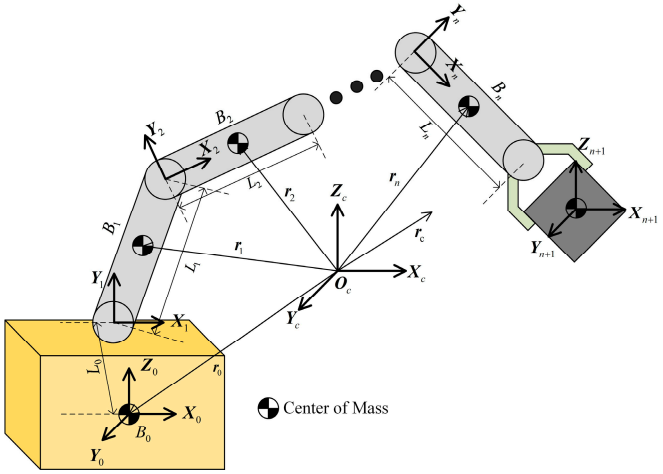


Figure 1. The diagram of a n-link space robot.

The inertia parameters of the space robot are considered known, while extreme temperature variations in practical space environments and fuel consumption can all contribute to the model uncertainties. Therefore, the parametric uncertainties are formally given as below:

$$\begin{cases} \boldsymbol{D}(\boldsymbol{q}) = \boldsymbol{D}_0(\boldsymbol{q}) + \Delta\boldsymbol{D}(\boldsymbol{q}) \\ \boldsymbol{H}(\boldsymbol{q}, \dot{\boldsymbol{q}}) = \boldsymbol{H}_0(\boldsymbol{q}, \dot{\boldsymbol{q}}) + \Delta\boldsymbol{H}(\boldsymbol{q}, \dot{\boldsymbol{q}}) \end{cases} \tag{2}$$

where $\boldsymbol{D}_0$, $\boldsymbol{H}_0$ denote the nominal values, and $\boldsymbol{D}$, $\boldsymbol{H}$ and $\Delta\boldsymbol{D}$, $\Delta\boldsymbol{H}$ denote the uncertainties of space robot system.

According to Equation (2), Equation (1) is reformulated to:

$$\boldsymbol{D}_0(\boldsymbol{q})\ddot{\boldsymbol{q}} + \boldsymbol{H}_0(\boldsymbol{q}, \dot{\boldsymbol{q}})\dot{\boldsymbol{q}} = \boldsymbol{\tau}(t) + \boldsymbol{O}_\tau \tag{3}$$

where $\boldsymbol{O}_\tau$ denotes the lumped uncertainties, including model uncertainties and external disturbances; this is represented by:

$$\boldsymbol{O}_\tau = \boldsymbol{\tau}_d(t) - \Delta\boldsymbol{D}(\boldsymbol{q})\ddot{\boldsymbol{q}} - \Delta\boldsymbol{H}(\boldsymbol{q}, \dot{\boldsymbol{q}})\dot{\boldsymbol{q}} \tag{4}$$

where $\boldsymbol{\tau}_d(t)$ represents the external disturbances.

To investigate the direct relationship between the lumped uncertainty and the system according to equation $\ddot{\boldsymbol{q}} = \boldsymbol{D}_0^{-1}(\boldsymbol{q})\boldsymbol{\tau}(t) - \boldsymbol{D}_0^{-1}(\boldsymbol{q})\boldsymbol{H}_0(\boldsymbol{q}, \dot{\boldsymbol{q}})\dot{\boldsymbol{q}} + \boldsymbol{\Gamma}_\tau$; the lumped uncertainties are reformulated as:

$$\boldsymbol{\Gamma}_\tau = \boldsymbol{D}_0^{-1}(\boldsymbol{q})\boldsymbol{\tau}_d(t) - \boldsymbol{D}_0^{-1}(\boldsymbol{q})\Delta\boldsymbol{D}(\boldsymbol{q})\ddot{\boldsymbol{q}} - \boldsymbol{D}_0^{-1}(\boldsymbol{q})\Delta\boldsymbol{H}(\boldsymbol{q}, \dot{\boldsymbol{q}})\dot{\boldsymbol{q}} \tag{5}$$

Assumption 1. *The positive definite matrix $\boldsymbol{D}(\boldsymbol{q})$ is reversible, which satisfies the design constraint:*

$$\zeta_0 \leq \|\boldsymbol{D}(\boldsymbol{q})\| \leq \zeta_1 \tag{6}$$

where ζ_0, ζ_1 are positive numbers.

Assumption 2. *The unknown uncertainties $\boldsymbol{\Gamma}_\tau$ in the system subject to supremum ρ with the following representation:*

$$|\boldsymbol{\Gamma}_\tau| \leq \rho = a_0 + a_1\|\boldsymbol{e}\| + a_2\|\dot{\boldsymbol{e}}\| \tag{7}$$

Defining the desired trajectory of system, $\boldsymbol{q}_d = [q_{d0}, q_{d1}, q_{d2}]^T$; thereby, the trajectory tracking error $\boldsymbol{e}$ is defined as $\boldsymbol{e} = \boldsymbol{q} - \boldsymbol{q}_d$ and relevant parameters a_0, a_1, a_2 are positive constants.

Note [32]: In control systems, control inputs usually do not involve acceleration, and they achieve the desired effect by regulating position and velocity. Equation (7) represents external uncertainties that primarily arise from changes in the system's position and velocity due to external disturbances, which subsequently impact trajectory tracking performance. Consequently, the unknown uncertainties in Equation (7) are expressed as a function of position and velocity.

Definition 1. *In this paper, the signum function is given by:*

$$sign(x) = \begin{cases} -1 & \text{if } x < 0 \\ 0 & \text{if } x = 0 \\ +1 & \text{if } x > 0 \end{cases} \tag{8}$$

Thus, the function $sig(x)^\alpha$ is defined as follows:

$$\begin{cases} sig(x)^\alpha = |x|^\alpha sign(x) \\ \dfrac{d(sig(x))}{dx} = \alpha|x|^{\alpha-1}sign(x)\dot{x} \end{cases} \tag{9}$$

Among input vectors $\boldsymbol{x} \in \boldsymbol{R}^{N\times 1}$ and $\alpha \geq 1$.

Definition 2. *(Finite-Time Theory) [33]. Consider a nonlinear system function satisfying:*

$$\dot{x}(t) = f(x(t)) \tag{10}$$

where $x(t) \in \boldsymbol{R}^n$ is the system state, $f : U \to \boldsymbol{R}^n$ is a continuous function defined on a domain $U \subset \boldsymbol{R}^n$ containing the origin, $\boldsymbol{0} \in \boldsymbol{R}^n$ denotes the zero vector, and x_0 represents the initial state.

Based on system (10), the following relevant preliminary is given:

Preliminary 1. *For the aforementioned nonlinear system, there reveals a positive definite function $V(x)$ defined on the domain U such that:*

$$\dot{V}(t) \leq -\sigma_1 V(t) - \sigma_2 V^\eta(t), \forall t \geq t_0 \tag{11}$$

Given positive constants σ_1, $\sigma_2 > 0$, $0 < \eta < 1$, the nonlinear system satisfies finite-time stability. Therefore, if $x(t)$ lies within the set $\Omega = \{x : V^{1-\eta}(t) < -\sigma_2/\sigma_1\}$, then it ensures that the closed-loop system converges to the equilibrium point in finite time, simultaneously settling time T satisfying:

$$T(t_0) \leq T_{\max} = \frac{1}{\sigma_1(1-\eta)} \ln \frac{\sigma_1 V^{1-\eta}(x_0) + \sigma_2}{\sigma_2} \tag{12}$$

3. Controller Design

3.1. Nonsingular Fast Terminal Sliding Mode Controller Design

For the space robot system shown in Figure 1, a novel sliding-mode surface is developed within the NFTSMC framework, and its formulation is given as follows:

$$\boldsymbol{s} = \boldsymbol{e} + b_1 sig(\boldsymbol{e})^{\gamma_1} + b_2 sig(\dot{\boldsymbol{e}})^{\gamma_2} \tag{13}$$

Remark 1. *Where b_1, b_2 are both positive numbers, $\gamma_2 \in (1,2)$ and γ_1 are the parameters of design surface ($\gamma_1 > \gamma_2$). The fractional-order terms of the proposed sliding-mode surface are all greater than one, which guarantees avoidance of singularities while ensuring finite-time stability. The linear term accelerates convergence in the region of small trajectory-tracking errors.*

The sliding surface Function (13) is differentiated with respect to time to obtain its time derivative:

$$\dot{\boldsymbol{s}} = \dot{\boldsymbol{e}} + b_1\gamma_1 |\boldsymbol{e}|^{\gamma_1 - 1}\dot{\boldsymbol{e}} + b_2\gamma_2 |\dot{\boldsymbol{e}}|^{\gamma_2 - 1}\ddot{\boldsymbol{e}} \tag{14}$$

As the error tends to zero, the sliding mode trajectories converge to the sliding surface ($\boldsymbol{s} = 0$). At this juncture, the control law generates a continuous, high-frequency equivalent control that effectively mitigates the impact of model uncertainties and disturbances, rendering the system's motion as if the lumped uncertainties did not exist.

$$\begin{aligned} &\dot{\boldsymbol{s}} = \dot{\boldsymbol{e}} + b_1\gamma_1 |\boldsymbol{e}|^{\gamma_1 - 1}\dot{\boldsymbol{e}} + b_2\gamma_2 |\dot{\boldsymbol{e}}|^{\gamma_2 - 1}\ddot{\boldsymbol{e}} = 0 \\ &\Rightarrow \dot{\boldsymbol{e}} + b_1\gamma_1 |\boldsymbol{e}|^{\gamma_1 - 1}\dot{\boldsymbol{e}} + b_2\gamma_2 |\dot{\boldsymbol{e}}|^{\gamma_2 - 1}(\ddot{\boldsymbol{q}} - \ddot{\boldsymbol{q}}_d) = 0 \\ &\Rightarrow \dot{\boldsymbol{e}} + b_1\gamma_1 |\boldsymbol{e}|^{\gamma_1 - 1}\dot{\boldsymbol{e}} + b_2\gamma_2 |\dot{\boldsymbol{e}}|^{\gamma_2 - 1}(\boldsymbol{D}_0^{-1}(\boldsymbol{q})(\boldsymbol{\tau}_{eq} - \boldsymbol{H}_0(\boldsymbol{q}, \dot{\boldsymbol{q}})\dot{\boldsymbol{q}}) - \ddot{\boldsymbol{q}}_d) = 0 \end{aligned} \tag{15}$$

Based on Equation (15), the equivalent control term $\boldsymbol{\tau}_{eq}$ is designed as:

$$\boldsymbol{\tau}_{eq} = \boldsymbol{D}_0(\boldsymbol{q}) \left[\ddot{\boldsymbol{q}}_d - \left(\frac{1}{b_2\gamma_2} |\dot{\boldsymbol{e}}|^{2-\gamma_2} + \frac{b_1\gamma_1}{b_2\gamma_2} |\boldsymbol{e}|^{\gamma_1 - 1} |\dot{\boldsymbol{e}}|^{2-\gamma_2} \right) sign(\dot{\boldsymbol{e}}) \right] + \boldsymbol{H}_0(\boldsymbol{q}, \dot{\boldsymbol{q}})\dot{\boldsymbol{q}} \tag{16}$$

Concurrently, the switching term $\boldsymbol{\tau}_{sw}$ is constructed according to a constant-rate reaching law $\dot{\boldsymbol{s}} = -\varepsilon \cdot sign(\boldsymbol{s})$:

$$\boldsymbol{\tau}_{sw} = -\boldsymbol{D}_0(\boldsymbol{q})[(\rho + \varepsilon) sign(\boldsymbol{s})] \tag{17}$$

where ε is a positive constant.

To mitigate external disturbances, a disturbance compensation term $\boldsymbol{\tau}_{ct}$ is introduced:

$$\boldsymbol{\tau}_{ct} = -\boldsymbol{D}_0(\boldsymbol{q}) N \boldsymbol{s} \tag{18}$$

where $N \geq 0$ refers to parameter of compensation term.

Based on the preceding derivation, the control law of the controller takes the following form:

$$\begin{aligned} \boldsymbol{\tau} &= \boldsymbol{\tau}_{eq} + \boldsymbol{\tau}_{sw} + \boldsymbol{\tau}_{ct} \\ &= \boldsymbol{\tau}_{eq} - \boldsymbol{D}_0(\boldsymbol{q})[(\rho + \varepsilon) sign(\boldsymbol{s})] - \boldsymbol{D}_0(\boldsymbol{q}) N \boldsymbol{s} \\ &= \boldsymbol{D}_0(\boldsymbol{q})[\ddot{\boldsymbol{q}}_d - (\tfrac{1}{b_2\gamma_2} |\dot{\boldsymbol{e}}|^{2-\gamma_2} + \tfrac{b_1\gamma_1}{b_2\gamma_2} |\boldsymbol{e}|^{\gamma_1 - 1} |\dot{\boldsymbol{e}}|^{2-\gamma_2}) sign(\dot{\boldsymbol{e}}) - (\rho + \varepsilon) sign(\boldsymbol{s}) - N\boldsymbol{s}] + \boldsymbol{H}_0(\boldsymbol{q}, \dot{\boldsymbol{q}})\dot{\boldsymbol{q}} \end{aligned} \tag{19}$$

3.2. Wavelet Neural Network Design

The design of space robot controller is inherently complex and challenging due to the presence of model uncertainties and nonlinear dynamics. These uncertainties primarily arise from factors such as solar wind, electromagnetic particle flows, and external disturbances. Finding solutions to these challenges is a key focus of ongoing research. Neural networks possess strong fitting capabilities and can approximate model uncertainties through continuous learning. Consequently, their application in space robot control has attracted increasing interest from researchers in recent years. A wavelet neural network (WNN) is a type of neural network that employs wavelet basis functions as its activation functions. Unlike radial basis function (RBF) networks, which typically use Gaussian basis functions, this paper adopts the Mexican hat function. By leveraging its multiscale transformation properties, the network can sensitively detect variations in overall uncertainty. By modifying the activation function, its unique characteristics can be effectively exploited to improve control performance.

This paper introduces a wavelet neural network (WNN), as shown in Figure 2, to estimate the upper bound of uncertainties. The WNN is favored for its strong approximation capability as well as its ease of implementation and learning. Unlike conventional neural networks, the WNN employs wavelet functions as activation units, leveraging their time-scale localization properties to provide a powerful approximation capability. Therefore, wavelet functions are selected in this study to address model uncertainty.

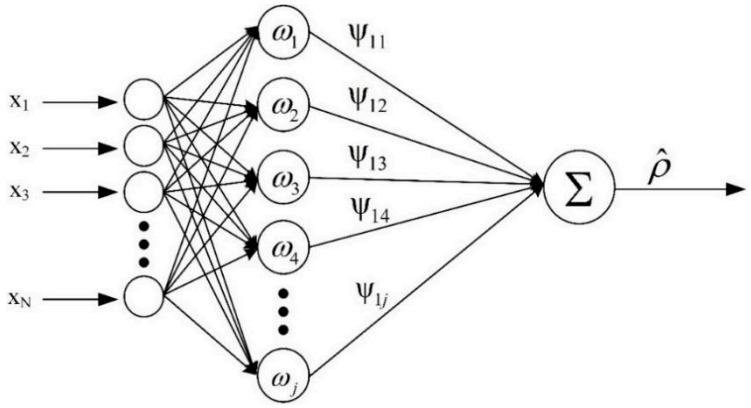


Figure 2. Wavelet neural network.

In the estimation of the lumped uncertainty term, the following assumptions are introduced:

$$\begin{cases} \boldsymbol{\rho} = \boldsymbol{\rho}^* + o \\ \tilde{\boldsymbol{\rho}} = \boldsymbol{\rho}^* - \hat{\boldsymbol{\rho}} \\ \boldsymbol{\rho}^* = \boldsymbol{\psi}^{*T}\boldsymbol{\omega}(\boldsymbol{x}, \boldsymbol{c}, \boldsymbol{b}) \\ \hat{\boldsymbol{\rho}} = \hat{\boldsymbol{\psi}}^T\boldsymbol{\omega}(\boldsymbol{x}, \boldsymbol{c}, \boldsymbol{b}) \\ \boldsymbol{\omega} = \prod_{i=1}^{N} \mathrm{f}\left(\dfrac{\boldsymbol{x}_i - \boldsymbol{c}_{ji}}{\boldsymbol{b}_{ji}}\right) \\ \mathrm{f}(z_{ji}) = \left(1 - z_{ji}^2\right)\exp\left(\frac{1}{2}z_{ji}^2\right) \end{cases} \tag{20}$$

In these formulas, $\boldsymbol{x} \in \boldsymbol{R}^{N\times 1}$ represents the network input. $\boldsymbol{c}$ denotes the translation parameter, and $\boldsymbol{b}$ is the scaling parameter. $\boldsymbol{\rho}^*$ expresses the WNN suitable architecture with o being a positive number. $\hat{\boldsymbol{\rho}}$ is defined as an estimation to model uncertainties $\boldsymbol{\rho}$. $\hat{\boldsymbol{\psi}}$ stands for the weighting variables. $\hat{\omega}$ is the wavelet function to fit nonlinear terms. $\boldsymbol{\psi}^*$ is suitable parameter of weighting variables.

Considering the WNN capability in estimating the model uncertainties, the switching term $\boldsymbol{\tau}_{sw}$ and the compensation term $\boldsymbol{\tau}_{ct}$ can be expressed as:

$$\begin{cases} \boldsymbol{\tau}_{sw} = -\boldsymbol{D}_0^{-1}(\boldsymbol{q})[(\hat{\boldsymbol{\rho}} + \varepsilon) sign(\boldsymbol{s})] \\ \boldsymbol{\tau}_{ct} = -\boldsymbol{D}_0^{-1}(\boldsymbol{q})\hat{\boldsymbol{N}}\boldsymbol{s} \end{cases} \tag{21}$$

The overall control law is reformulated as follows:

$$\begin{aligned} \boldsymbol{\tau} &= \boldsymbol{\tau}_{eq} + \boldsymbol{\tau}_{sw} + \boldsymbol{\tau}_{ct} \\ &= \boldsymbol{D}_0(\boldsymbol{q})[\ddot{\boldsymbol{q}}_d - (\tfrac{1}{b_2\gamma_2}|\dot{\boldsymbol{e}}|^{2-\gamma_2} + \tfrac{b_1\gamma_1}{b_2\gamma_2}|\boldsymbol{e}|^{\gamma_1-1}|\dot{\boldsymbol{e}}|^{2-\gamma_2}) sign(\dot{\boldsymbol{e}}) - (\hat{\boldsymbol{\rho}} + \varepsilon) sign(\boldsymbol{s}) - \hat{\boldsymbol{N}}\boldsymbol{s}] + \boldsymbol{H}_0(\boldsymbol{q}, \dot{\boldsymbol{q}})\dot{\boldsymbol{q}} \end{aligned} \tag{22}$$

The adaptive parameters are defined as follows:

$$\begin{cases} \dot{\hat{\boldsymbol{\psi}}} = b_2\gamma_2 n_W |\dot{\boldsymbol{e}}|^{\gamma_2-1} |\boldsymbol{s}| \boldsymbol{\omega}(\boldsymbol{x}, \boldsymbol{c}, \boldsymbol{b}) \\ \dot{\hat{\boldsymbol{N}}} = b_2\gamma_2 n_N |\dot{\boldsymbol{e}}|^{\gamma_2-1} \boldsymbol{s}^{\mathrm{T}}\boldsymbol{s} \end{cases} \tag{23}$$

With n_W and n_N are relevant positive parameters.

4. Stability Analysis

Considering the NFTSMC surface, the Lyapunov function is selected as $V_1 = \frac{1}{2}\boldsymbol{s}^2$. Equation (14) can transform into the following form:

$$\begin{aligned} \dot{\boldsymbol{s}} &= \dot{\boldsymbol{e}} + b_1\gamma_1|\boldsymbol{e}|^{\gamma_1-1}\dot{\boldsymbol{e}} + b_2\gamma_2|\dot{\boldsymbol{e}}|^{\gamma_2-1}(\ddot{\boldsymbol{q}} - \ddot{\boldsymbol{q}}_d) \\ &= \dot{\boldsymbol{e}} + b_1\gamma_1|\boldsymbol{e}|^{\gamma_1-1}\dot{\boldsymbol{e}} + b_2\gamma_2|\dot{\boldsymbol{e}}|^{\gamma_2-1}(\boldsymbol{D}_0^{-1}(\boldsymbol{q})(\boldsymbol{\Gamma}_\tau + \boldsymbol{\tau} - \boldsymbol{H}_0(\boldsymbol{q}, \dot{\boldsymbol{q}})\dot{\boldsymbol{q}}) - \ddot{\boldsymbol{q}}_d) \\ &= \dot{\boldsymbol{e}} + b_1\gamma_1|\boldsymbol{e}|^{\gamma_1-1}\dot{\boldsymbol{e}} + b_2\gamma_2|\dot{\boldsymbol{e}}|^{\gamma_2-1}(\boldsymbol{D}_0^{-1}(\boldsymbol{q})(\boldsymbol{\Gamma}_\tau + \boldsymbol{\tau}_{eq} + \boldsymbol{\tau}_{sw} + \boldsymbol{\tau}_{ct} - \boldsymbol{H}_0(\boldsymbol{q}, \dot{\boldsymbol{q}})\dot{\boldsymbol{q}}) - \ddot{\boldsymbol{q}}_d) \\ &= b_2\gamma_2|\dot{\boldsymbol{e}}|^{\gamma_2-1}[\boldsymbol{\Gamma}_\tau - (\rho + \varepsilon) sign(\boldsymbol{s}) - N\boldsymbol{s}] \end{aligned} \tag{24}$$

Take the derivative of the Lyapunov function V_1 with respect to time t:

$$\begin{aligned} \dot{V}_1 &= \boldsymbol{s}\dot{\boldsymbol{s}} \\ &= \boldsymbol{s}\Big(b_2\gamma_2|\boldsymbol{e}|^{\gamma_2-1}[\boldsymbol{\Gamma}_\tau - (\rho + \varepsilon) sign(\boldsymbol{s}) - N\boldsymbol{s}]\Big) \\ &= \big[\boldsymbol{\Gamma}_\tau\boldsymbol{s} - (\rho + \varepsilon)\boldsymbol{s} - N\boldsymbol{s}^2\big] b_2\gamma_2|\boldsymbol{e}|^{\gamma_2-1} \\ &\le \big[|\boldsymbol{\Gamma}_\tau| \cdot |\boldsymbol{s}| - (\rho + \varepsilon) \cdot |\boldsymbol{s}| - N\boldsymbol{s}^2\big] b_2\gamma_2|\boldsymbol{e}|^{\gamma_2-1} \\ &\le \big(|\boldsymbol{\Gamma}_\tau - \rho| \cdot |\boldsymbol{s}| - \varepsilon|\boldsymbol{s}| - N\boldsymbol{s}^2\big) b_2\gamma_2|\boldsymbol{e}|^{\gamma_2-1} \end{aligned} \tag{25}$$

Under Assumption 2, the expression $\dot{V}_1$ can be simplified as follows:

$$\begin{aligned} \dot{V}_1 &\le \big(|\boldsymbol{\Gamma}_\tau - \rho| \cdot |\boldsymbol{s}| - \varepsilon|\boldsymbol{s}| - N\boldsymbol{s}^2\big) b_2\gamma_2|\boldsymbol{e}|^{\gamma_2-1} \\ &\le \big(-\varepsilon|\boldsymbol{s}| - N\boldsymbol{s}^2\big) b_2\gamma_2|\boldsymbol{e}|^{\gamma_2-1} \le 0 \end{aligned} \tag{26}$$

Based on Preliminary 1, Equation (26) can be transformed into the following form:

$$\begin{aligned} \dot{V}_1 &\le \big(-\varepsilon|\boldsymbol{s}| - N\boldsymbol{s}^2\big) b_2\gamma_2|\boldsymbol{e}|^{\gamma_2-1} \\ &\le -b_2\gamma_2|\boldsymbol{e}|^{\gamma_2-1}N\boldsymbol{s}^2 - b_2\gamma_2|\boldsymbol{e}|^{\gamma_2-1}\varepsilon|\boldsymbol{s}| \\ &\le -k_1V_1 - k_2V_1^{\frac{1}{2}} \end{aligned} \tag{27}$$

where $k_1 = 2b_2\gamma_2|\boldsymbol{e}|^{\gamma_2-1}N$ and $k_2 = \sqrt{2}\varepsilon b_2\gamma_2|\boldsymbol{e}|^{\gamma_2-1}$ are both positive numbers.

From Preliminary 1, it can be deduced that the finite-time convergence characterized by t_r ensures that the sliding mode variable $\dot{\boldsymbol{s}}$ converges to zero.

$$\dot{V}_1 \le -k_1V_1 - k_2V_1^{\frac{1}{2}} \tag{28}$$

$$dt \leq \frac{dV_1}{-k_1 V_1 - k_2 V_1^{\frac{1}{2}}} \tag{29}$$

By integrating both sides of the inequality, the following expression for the convergence time is obtained:

$$\int_0^{t_r} t \leq \int_{V_1(0)}^{V_1(t_r)} \frac{dV_1}{-k_1 V_1 - k_2 V_1^{\frac{1}{2}}} \Rightarrow t_r \leq \frac{2}{k_1} \ln\left(\frac{k_1 V_1^{\frac{1}{2}} + k_2}{k_2}\right) \tag{30}$$

Through the aforementioned rigorous analysis, the feasibility of the NFTSMC strategy is established, thereby verifying that the designed sliding surface guarantees finite-time stabilization of the space robot system.

The WNN is employed to modify the control law, and the corresponding Lyapunov function V_2 can be expressed as follows:

$$V_2 = V_1 + \frac{1}{2n_W}\tilde{\boldsymbol{\psi}}^{\boldsymbol{T}}\tilde{\boldsymbol{\psi}} + \frac{1}{2n_N}\tilde{\boldsymbol{N}}^{\boldsymbol{T}}\tilde{\boldsymbol{N}} \tag{31}$$

where $\tilde{\boldsymbol{\psi}}$=$\boldsymbol{\psi}^{*} - \hat{\boldsymbol{\psi}}$ and $\tilde{\boldsymbol{N}}$=$\hat{\boldsymbol{N}} - \boldsymbol{N}$.

V_2 is differentiated with respect to time t:

$$\begin{aligned} \dot{V}_2 &= \dot{V}_1 + \tfrac{1}{n_W}\tilde{\boldsymbol{\psi}}^{\boldsymbol{T}}\left(\dot{\boldsymbol{\psi}}^{*} - \dot{\hat{\boldsymbol{\psi}}}\right) + \tfrac{1}{n_N}\tilde{\boldsymbol{N}}^{\boldsymbol{T}}\left(\dot{\hat{\boldsymbol{N}}} - \dot{\boldsymbol{N}}\right) \\ &= \dot{V}_1 - \tfrac{1}{n_W}\tilde{\boldsymbol{\psi}}^{\boldsymbol{T}}\dot{\hat{\boldsymbol{\psi}}} + \tfrac{1}{n_N}\tilde{\boldsymbol{N}}^{\boldsymbol{T}}\dot{\hat{\boldsymbol{N}}} \end{aligned} \tag{32}$$

By virtue of the WNN's ability to estimate lumped uncertainties, the overall control law is given by:

$$\begin{aligned} \boldsymbol{\tau} &= \boldsymbol{\tau}_{eq} + \boldsymbol{\tau}_{sw} + \boldsymbol{\tau}_{ct} \\ &= \boldsymbol{D}_0(\boldsymbol{q})[\ddot{\boldsymbol{q}}_d - \tfrac{1}{b_2\gamma_2}|\dot{\boldsymbol{e}}|^{2-\gamma_2}(1 + b_1\gamma_1|\boldsymbol{e}|^{\gamma_1 - 1})sign(\dot{\boldsymbol{e}}) - (\hat{\boldsymbol{\rho}} + \varepsilon)sign(\boldsymbol{s}) - \hat{\boldsymbol{N}}\boldsymbol{s}] + \boldsymbol{H}_0(\boldsymbol{q}, \dot{\boldsymbol{q}})\dot{\boldsymbol{q}} \end{aligned} \tag{33}$$

The new sliding mode surface $\dot{\boldsymbol{s}}(t)$ is defined as follows:

$$\begin{aligned} \dot{\boldsymbol{s}} &= \left(1 + b_1\gamma_1|\boldsymbol{e}|^{\gamma_1 - 1}\right)\dot{\boldsymbol{e}} + b_2\gamma_2|\dot{\boldsymbol{e}}|^{\gamma_2 - 1}(\boldsymbol{D}_0^{-1}(\boldsymbol{q})(\boldsymbol{\Gamma}_\tau + \boldsymbol{\tau}_{eq} + \boldsymbol{\tau}_{sw} + \boldsymbol{\tau}_{ct} + -\boldsymbol{H}_0(\boldsymbol{q}, \dot{\boldsymbol{q}})\dot{\boldsymbol{q}}) - \ddot{\boldsymbol{q}}_d) \\ &= b_2\gamma_2|\dot{\boldsymbol{e}}|^{\gamma_2 - 1}\left[\boldsymbol{\Gamma}_\tau - (\hat{\boldsymbol{\rho}} + \varepsilon)sign(\boldsymbol{s}) - \hat{\boldsymbol{N}}\boldsymbol{s}\right] \end{aligned} \tag{34}$$

From the new sliding mode surface $\dot{\boldsymbol{s}}(t)$, it follows that $\dot{V}_1$:

$$\dot{V}_1 = b_2\gamma_2|\boldsymbol{e}|^{\gamma_2 - 1}\left[\boldsymbol{\Gamma}_\tau\boldsymbol{s} - (\hat{\boldsymbol{\rho}} + \varepsilon)\boldsymbol{s} - \hat{\boldsymbol{N}}\boldsymbol{s}^2\right] \tag{35}$$

Then, the $\dot{V}_2$ is rewritten as:

$$\dot{V}_2 = b_2\gamma_2|\boldsymbol{e}|^{\gamma_2 - 1}\left[\boldsymbol{\Gamma}_\tau\boldsymbol{s} - (\hat{\boldsymbol{\rho}} + \varepsilon)\boldsymbol{s} - \hat{\boldsymbol{N}}\boldsymbol{s}^2\right] - \frac{1}{n_W}\tilde{\boldsymbol{\psi}}^{\boldsymbol{T}}\dot{\hat{\boldsymbol{\psi}}} + \frac{1}{n_N}\tilde{\boldsymbol{N}}^{\boldsymbol{T}}\dot{\hat{\boldsymbol{N}}} \tag{36}$$

According to $\boldsymbol{s} \leq |\boldsymbol{s}|$, $\dot{V}_2$ could be expressed as follows:

$$\begin{aligned} \dot{V}_2 &\leq b_2\gamma_2|\boldsymbol{e}|^{\gamma_2 - 1}\left[[\boldsymbol{\Gamma}_\tau - (\hat{\boldsymbol{\rho}} + \varepsilon)]|\boldsymbol{s}| - \hat{\boldsymbol{N}}\boldsymbol{s}^2\right] - \tfrac{1}{n_W}\tilde{\boldsymbol{\psi}}^{\boldsymbol{T}}\dot{\hat{\boldsymbol{\psi}}} + \tfrac{1}{n_N}\tilde{\boldsymbol{N}}^{\boldsymbol{T}}\dot{\hat{\boldsymbol{N}}} \\ &\leq b_2\gamma_2|\boldsymbol{e}|^{\gamma_2 - 1}\left[[|\boldsymbol{\Gamma}_\tau| - (\hat{\boldsymbol{\rho}} + \varepsilon)]|\boldsymbol{s}| - \hat{\boldsymbol{N}}\boldsymbol{s}^2\right] - \tfrac{1}{n_W}\tilde{\boldsymbol{\psi}}^{\boldsymbol{T}}\dot{\hat{\boldsymbol{\psi}}} + \tfrac{1}{n_N}\tilde{\boldsymbol{N}}^{\boldsymbol{T}}\dot{\hat{\boldsymbol{N}}} \end{aligned} \tag{37}$$

From Equation (7) ($|\boldsymbol{\Gamma}_\tau| \leq \boldsymbol{\rho}$), it follows that Equation (37) can be simplified to:

$$\dot{V}_2 \le b_2\gamma_2|\boldsymbol{e}|^{\gamma_2-1}\left[\boldsymbol{\rho}|\boldsymbol{s}| - \hat{\boldsymbol{\rho}}|\boldsymbol{s}| - \varepsilon|\boldsymbol{s}| - \hat{\boldsymbol{N}}\boldsymbol{s}^2\right] - \frac{1}{n_W}\tilde{\boldsymbol{\psi}}^{\mathrm{T}}\dot{\hat{\boldsymbol{\psi}}} + \frac{1}{n_N}\tilde{\boldsymbol{N}}^{\mathrm{T}}\dot{\hat{\boldsymbol{N}}} \tag{38}$$

From Equation (20) $\boldsymbol{\rho} = \boldsymbol{\rho} * + o$, it follows that Equation (38) can be simplified to:

$$\begin{aligned}\dot{V}_2 &\le b_2\gamma_2|\boldsymbol{e}|^{\gamma_2-1}\left[(\boldsymbol{\rho}^* + o)|\boldsymbol{s}| - \hat{\boldsymbol{\rho}}|\boldsymbol{s}| - \varepsilon|\boldsymbol{s}| - \hat{\boldsymbol{N}}\boldsymbol{s}^2\right] - \tfrac{1}{n_W}\tilde{\boldsymbol{\psi}}^{\mathrm{T}}\dot{\hat{\boldsymbol{\psi}}} + \tfrac{1}{n_N}\tilde{\boldsymbol{N}}^{\mathrm{T}}\dot{\hat{\boldsymbol{N}}} \\ &\le b_2\gamma_2|\boldsymbol{e}|^{\gamma_2-1}\left[(\boldsymbol{\rho}^* - \hat{\boldsymbol{\rho}})|\boldsymbol{s}| + (o-\varepsilon)|\boldsymbol{s}| - \hat{\boldsymbol{N}}\boldsymbol{s}^2\right] - \tfrac{1}{n_W}\tilde{\boldsymbol{\psi}}^{\mathrm{T}}\dot{\hat{\boldsymbol{\psi}}} + \tfrac{1}{n_N}\tilde{\boldsymbol{N}}^{\mathrm{T}}\dot{\hat{\boldsymbol{N}}}\end{aligned} \tag{39}$$

With $\mu_{\mathrm{T}} = o - \varepsilon$, a positive small constant.

By Equation (20), $\boldsymbol{\rho}^* = \boldsymbol{\psi}^{*T}\boldsymbol{\omega}(\boldsymbol{x},\boldsymbol{c},\boldsymbol{b})$ and $\hat{\boldsymbol{\rho}} = \hat{\boldsymbol{\psi}}^{T}\boldsymbol{\omega}(\boldsymbol{x},\boldsymbol{c},\boldsymbol{b})$, which leads to further simplification:

$$\begin{aligned}\dot{V}_2 &\le b_2\gamma_2|\boldsymbol{e}|^{\gamma_2-1}\left[\left[\boldsymbol{\psi}^{*T}\boldsymbol{\omega}(\boldsymbol{x},\boldsymbol{c},\boldsymbol{b}) - \hat{\boldsymbol{\psi}}^{T}\boldsymbol{\omega}(\boldsymbol{x},\boldsymbol{c},\boldsymbol{b})\right]|\boldsymbol{s}| + (o-\varepsilon)|\boldsymbol{s}| - \hat{\boldsymbol{N}}\boldsymbol{s}^2\right] - \tfrac{1}{n_W}\tilde{\boldsymbol{\psi}}^{\mathrm{T}}\dot{\hat{\boldsymbol{\psi}}} + \tfrac{1}{n_N}\tilde{\boldsymbol{N}}^{\mathrm{T}}\dot{\hat{\boldsymbol{N}}} \\ &\le b_2\gamma_2|\boldsymbol{e}|^{\gamma_2-1}\left[(\boldsymbol{\psi}^{*T} - \hat{\boldsymbol{\psi}}^{T})\boldsymbol{\omega}(\boldsymbol{x},\boldsymbol{c},\boldsymbol{b})|\boldsymbol{s}| - \mu_{\mathrm{T}}|\boldsymbol{s}| - \hat{\boldsymbol{N}}\boldsymbol{s}^2\right] - \tfrac{1}{n_W}\tilde{\boldsymbol{\psi}}^{\mathrm{T}}\dot{\hat{\boldsymbol{\psi}}} + \tfrac{1}{n_N}\tilde{\boldsymbol{N}}^{\mathrm{T}}\dot{\hat{\boldsymbol{N}}} \\ &\le b_2\gamma_2\tilde{\boldsymbol{\psi}}^{\mathrm{T}}\boldsymbol{\omega}(\boldsymbol{x},\boldsymbol{c},\boldsymbol{b})|\boldsymbol{e}|^{\gamma_2-1}|\boldsymbol{s}| - b_2\gamma_2\mu_{\mathrm{T}}|\boldsymbol{e}|^{\gamma_2-1}|\boldsymbol{s}| - b_2\gamma_2\hat{\boldsymbol{N}}|\boldsymbol{e}|^{\gamma_2-1}\boldsymbol{s}^2 - \tfrac{1}{n_W}\tilde{\boldsymbol{\psi}}^{\mathrm{T}}\dot{\hat{\boldsymbol{\psi}}} + \tfrac{1}{n_N}(\hat{\boldsymbol{N}} - \boldsymbol{N})\dot{\hat{\boldsymbol{N}}}\end{aligned} \tag{40}$$

By adjusting Equation (40), $\dot{V}_2$ can be transformed into:

$$\begin{aligned}&\dot{V}_2 \le \tilde{\boldsymbol{\psi}}^{T}\left(b_2\gamma_2\boldsymbol{\omega}(\boldsymbol{x},\boldsymbol{c},\boldsymbol{b})|\boldsymbol{e}|^{\gamma_2-1}|\boldsymbol{s}| - \tfrac{1}{n_W}\dot{\hat{\boldsymbol{\psi}}}\right) + \hat{\boldsymbol{N}}\left(\tfrac{1}{n_N}\dot{\hat{\boldsymbol{N}}} - b_2\gamma_2|\boldsymbol{e}|^{\gamma_2-1}\boldsymbol{s}^2\right) \\ &-b_2\gamma_2\mu_{\mathrm{T}}|\boldsymbol{e}|^{\gamma_2-1}|\boldsymbol{s}| - \tfrac{1}{n_N}\boldsymbol{N}\dot{\hat{\boldsymbol{N}}}\end{aligned} \tag{41}$$

According to Equation (23), the $b_2\gamma_2\boldsymbol{\omega}(\boldsymbol{x},\boldsymbol{c},\boldsymbol{b})|\boldsymbol{e}|^{\gamma_2-1}|\boldsymbol{s}| - \frac{1}{n_W}\dot{\hat{\boldsymbol{\psi}}} = 0$ and $\frac{1}{n_N}\dot{\hat{\boldsymbol{N}}} - b_2\gamma_2|\boldsymbol{e}|^{\gamma_2-1}\boldsymbol{s}^2 = 0$, $\dot{V}_2$ can be simplified to:

$$\begin{aligned}\dot{V}_2 &\le -\tfrac{1}{n_N}\boldsymbol{N}\dot{\hat{\boldsymbol{N}}} - b_2\gamma_2\mu_{\mathrm{T}}|\boldsymbol{e}|^{\gamma_2-1}|\boldsymbol{s}| \\ &\le -b_2\gamma_2\boldsymbol{N}|\dot{\boldsymbol{e}}|^{\gamma_2-1}\boldsymbol{s}^2 - b_2\gamma_2\mu_{\mathrm{T}}|\boldsymbol{e}|^{\gamma_2-1}|\boldsymbol{s}| \\ &\le 0\end{aligned} \tag{42}$$

The above proof completes the proof of Preliminary 1, thereby establishing that the trajectory tracking errors converge to the equilibrium point within finite time.

5. Numerical Simulations

To further substantiate the effectiveness of the proposed NFTSMC-WNN strategy, numerical simulations were conducted on a two-link floating space robot system in a complex space environment.

The inertia parameters used in the dynamic model are given in Table 1:

Table 1. Inertial parameters.

Description	Symbols	Values
Length (m)	$L_0,\ L_1,\ L_2$	1, 1, 1
Center of mass (m)	$L_{c1},\ L_{c2}$	0.5, 0.5
Mass (kg)	$m_0,\ m_1,\ m_2$	40, 4, 3
Inertia (kg·m^2)	$I_0,\ I_1,\ I_2$	16.67, 1.5, 1.5

The proposed simulation parameters are given as follows:

$b_1 = 1, b_2 = 1, \gamma_1 = 2, \gamma_2 = \frac{5}{3}, N = 20, a_0 = 1, a_1 = 2.2, a_2 = 2.8, \boldsymbol{x} = [\boldsymbol{e}; \dot{\boldsymbol{e}}; \boldsymbol{s}], b = 2.$

In this paper, the parameters are selected according to the system model and simulation conditions. The control performance of the proposed algorithm when the parameter values vary is illustrated in Figure 3.

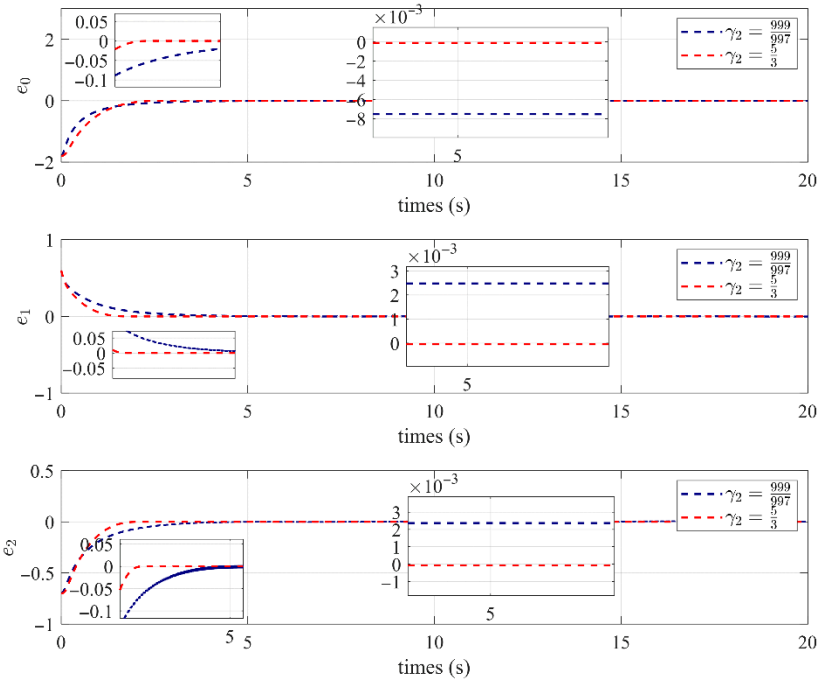


Figure 3. Tracking errors under different parameters.

Figure 3 compares the tracking errors obtained using the parameters set out in this paper with those obtained using different parameter settings. Under the parameters adopted in this study, it can be seen that the system achieves a shorter convergence time and higher tracking accuracy.

The desired trajectory tracking is as follows:

$$\boldsymbol{q}_d = \begin{bmatrix} q_{d0} \\ q_{d1} \\ q_{d2} \end{bmatrix} = \begin{bmatrix} \frac{5}{4} - \frac{7}{5}e^{-t} + \frac{7}{20}e^{-4t} \\ \frac{27}{20} + e^{-t} + \frac{1}{4}e^{-4t} \\ \frac{11}{20} + e^{-t} - \frac{1}{4}e^{-4t} \end{bmatrix} \tag{43}$$

Taking into account the presence of external disturbances, the disturbance $\boldsymbol{\tau}_d$ is defined as follows:

$$\boldsymbol{\tau}_d = \begin{bmatrix} \tau_{0d} \\ \tau_{1d} \\ \tau_{2d} \end{bmatrix} = \begin{bmatrix} 0.5\sin(t) + 0.5\sin(200\pi t) \\ 0.5\cos(t) - 0.5\sin(200\pi t) \\ 0.5\cos(t) - 0.5\cos(200\pi t) \end{bmatrix} \tag{44}$$

And model uncertainties $\boldsymbol{D}_0(\boldsymbol{q})$, $\boldsymbol{H}_0(\boldsymbol{q}, \dot{\boldsymbol{q}})$ are represented by $\boldsymbol{D}_0(\boldsymbol{q}) = 0.8\boldsymbol{D}(\boldsymbol{q})$ and $\boldsymbol{H}_0(\boldsymbol{q}, \dot{\boldsymbol{q}}) = 0.8\boldsymbol{H}(\boldsymbol{q}, \dot{\boldsymbol{q}})$. Then, (2) can be transformed into:

$$\begin{cases} \boldsymbol{D}(\boldsymbol{q}) = 0.8\boldsymbol{D}(\boldsymbol{q}) + \Delta\boldsymbol{D}(\boldsymbol{q}) \\ \boldsymbol{H}(\boldsymbol{q}, \dot{\boldsymbol{q}}) = 0.8\boldsymbol{H}(\boldsymbol{q}, \dot{\boldsymbol{q}}) + \Delta\boldsymbol{H}(\boldsymbol{q}, \dot{\boldsymbol{q}}) \end{cases} \tag{45}$$

where $\Delta\boldsymbol{D}(\boldsymbol{q}) = 0.2\boldsymbol{D}(\boldsymbol{q})$ and $\Delta\boldsymbol{H}(\boldsymbol{q}, \dot{\boldsymbol{q}}) = 0.2\boldsymbol{H}(\boldsymbol{q}, \dot{\boldsymbol{q}})$.

5.1. Case 1

To validate the effectiveness of the proposed control strategy, simulations are conducted under Case 1. The results, presented below, provide a comparison between the

proposed NFTSMC strategy and the TSMC approach from reference [34]. Simulation results obtained with the model-based controller in the absence of lumped uncertainties are shown in Figures 3 and 4. Figure 3 presents the trajectory tracking of proposed NFTSMC strategy and TSMC approach under the same initial state $\boldsymbol{q}(0) = [2, 2, 2]^{\mathrm{T}}$. Figure 4 shows the trajectory tracking errors of proposed control strategy.

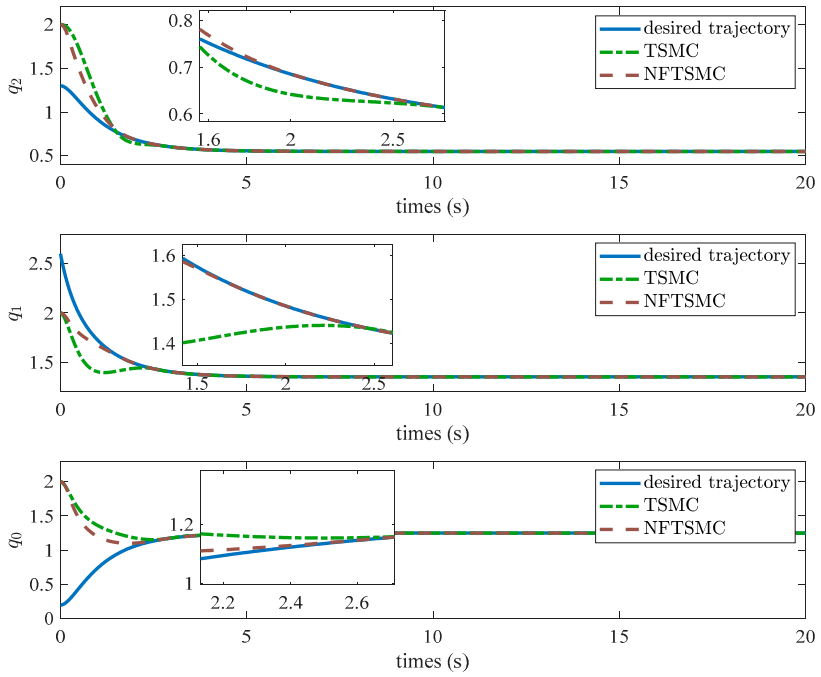


Figure 4. Trajectory tracking.

Figure 4 presents the tracking performance of the model-based NFTSMC and TSMC under the given initial state $\boldsymbol{q}(0) = [2, 2, 2]^{\mathrm{T}}$. During the 20 s simulation, both the TSMC and the proposed NFTSMC strategies enable the space robot system to converge to the equilibrium point within a finite time of $T = 2$ s, thereby confirming the effectiveness of the NFTSMC approach. Furthermore, as shown in Figure 3, the NFTSMC achieves faster convergence 0.2~0.5 s than the conventional TSMC, representing an approximate 19.23% improvement.

Figure 5 presents a comparison of tracking errors results under the same initial error states $\boldsymbol{e}(0) = [2, 2, 2]^{\mathrm{T}}$; the convergence time achieved by the NFTSMC method is 2.7 s, 1.8 s, 2.1 s, which is shorter than that of the TSMC at 3.6 s, 3.7 s, 2.9 s. Under identical initial errors, the proposed NFTSMC exhibits faster convergence to the equilibrium state than that under TSMC, particularly as the tracking errors approach zero. As shown in Figures 4 and 5, the proposed NFTSMC strategy achieves faster finite-time convergence compared with the conventional TSMC. This observation directly validates the key characteristic of rapid finite-time convergence inherent to the proposed control strategy.

As shown in Table 2, the error convergence rate of nonsingular fast terminal sliding mode control (NFTSMC) is significantly better than that of traditional terminal sliding mode control (TSMC). There is a maximum improvement of 51.35% in the convergence rate of each joint, and an improvement of 34.65% in overall convergence performance. TSMC is subject to inherent singularity issues, resulting in slow convergence rates and failure to meet real-time safety control requirements for spatial robots. The control strategy proposed in this paper therefore adopts NFTSMC as the basic sliding mode framework, avoiding singularity issues while enhancing the system's dynamic response and tracking control performance.

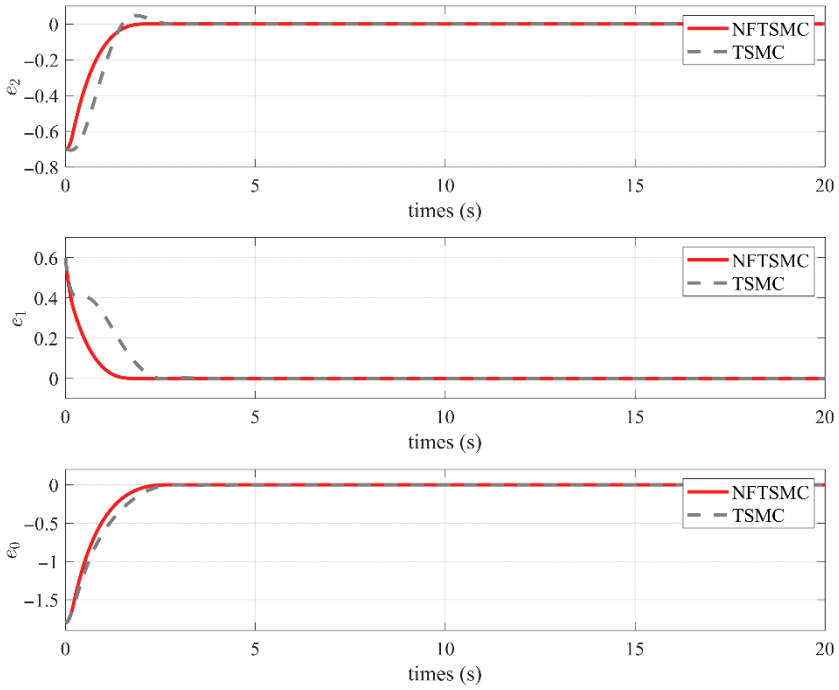


Figure 5. Trajectory tracking errors.

Table 2. Comparison of convergence time between TSMC and the NFTSMC.

Joint	Controller	Convergence Time (s)	Improvement (%)	Overall Improvements (%)
q_0	TSMC	3.6	25	34.65
	NFTSMC	2.7		
q_1	TSMC	3.7	51.35	
	NFTSMC	1.8		
q_2	TSMC	2.9	27.59	
	NFTSMC	2.1		

Figure 6 shows a comparison of tracking errors between the constant rate reaching law and high-order sliding mode control (HOSMC). As can be seen from the figure, the constant rate reaching law enables the proposed control algorithm in smaller tracking errors and better tracking accuracy than with HOSMC alone. However, a drawback of this approach is that it can cause slight oscillations. In contrast, HOSMC's core advantage is its ability to effectively suppress oscillation issues inherent in sliding mode control, achieving smoother control performance. However, this approach has a more complex structure, incurs a higher computational burden and has a greater tracking error than the constant rate reaching law. Consequently, it has shortcomings in terms of tracking accuracy and control efficiency. Based on the above comparison of characteristics, this study introduces a control scheme based on the constant rate reaching law within a high-order sliding mode framework. This approach circumvents the performance limitations of single control methods and avoids unnecessary control complexity. This makes it more suitable for scenarios with limited computational resources and high tracking accuracy and real-time performance requirements.

As presented in Table 3, compared to HOSMC, the constant rate reaching law exhibits only a slight delay of 1.97% in convergence time, yet achieves a significant improvement of 96.77% in tracking accuracy. In most space robotics operations, maintaining reliable steady-state tracking accuracy is generally more important than achieving a slight improvement in transient convergence speed. Furthermore, the constant-speed arrival law features a

simpler structure and lower computational complexity, which facilitates its implementation in space systems with limited resources. After comprehensive consideration of the above analysis, the constant-speed arrival law was selected as the control scheme. Based on the aforementioned analysis, this paper selects the high-order sliding mode control using a constant-rate convergence criterion as the control scheme.

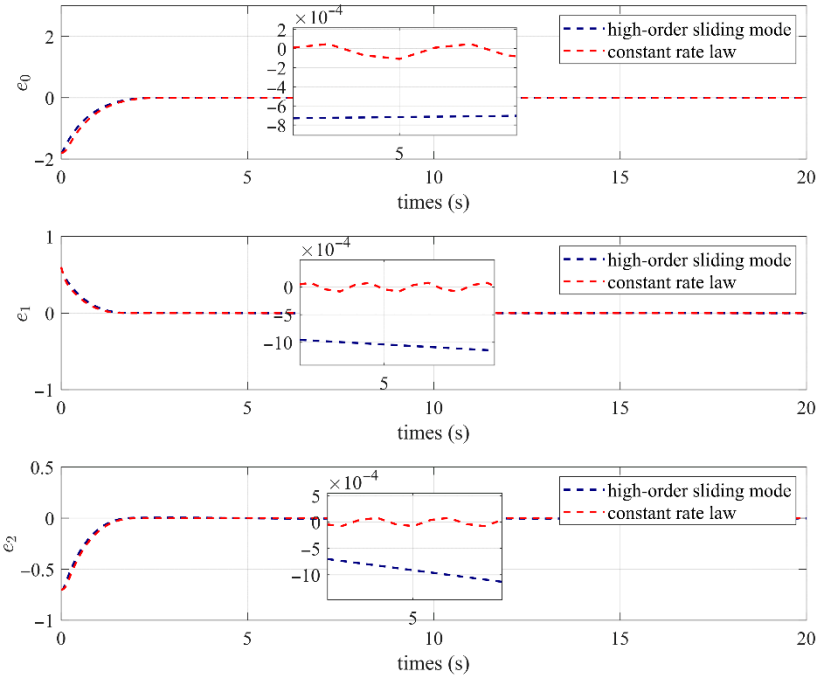


Figure 6. Tracking error comparisons with Higher-Order Sliding Mode Controller.

Table 3. Tracking performance comparisons with Higher-Order Sliding Mode Controller.

Joint	Controller	Convergence Time (s)	Percentage (%)	Mean Error (rad)	Percentage (%)
q_0	HOSMC Proposed	2.58 2.67	−4.65%	4.1325×10^{-4} 2.4272×10^{-5}	94.13%
q_1	HOSMC Proposed	1.8 1.76	2.22%	9.7804×10^{-4} 2.038×10^{-5}	97.92%
q_2	HOSMC Proposed	2.02 2.09	−3.47%	1.0822×10^{-3} 1.8721×10^{-5}	98.27%

5.2. Case 2

Although stability of the space robot system is guaranteed under the same initial state $\boldsymbol{q}(0) = [2,2,2]^{\mathrm{T}}$, this alone is insufficient to demonstrate the generality of the proposed strategy. To further validate the feasibility of the finite-time-based NFTSMC strategy under arbitrary initial states, simulations were conducted under three different initial states: $\boldsymbol{q}(0) = [1.5,1.5,1.5]^{\mathrm{T}}$, $\boldsymbol{q}(0) = [2,2,2]^{\mathrm{T}}$ and $\boldsymbol{q}(0) = [2.5,2.5,2.5]^{\mathrm{T}}$. Figure 7 illustrates the trajectory tracking performance under the NFTSMC method for three different initial states. Figure 8 presents the corresponding trajectory tracking errors for the three different initial error states $\boldsymbol{e}(0) = [1.5,1.5,1.5]^{\mathrm{T}}$, $\boldsymbol{e}(0) = [2,2,2]^{\mathrm{T}}$ and $\boldsymbol{e}(0) = [2.5,2.5,2.5]^{\mathrm{T}}$.

As shown in Figures 7 and 8, under different initial states, the trajectories successfully track the desired trajectories and the tracking errors converge to zero within finite-time. Specifically, Figure 7, under $\boldsymbol{q}(0) = [1.5,1.5,1.5]^{\mathrm{T}}$, indicates that the convergence time is approximately 2 s; under $\boldsymbol{q}(0) = [2,2,2]^{\mathrm{T}}$, the convergence time is around 1.8 s; under $\boldsymbol{q}(0) = [2.5,2.5,2.5]^{\mathrm{T}}$, the convergence time is around 1.83 s. Figure 8 describes the tracking

performance of trajectory tracking errors under different error states. Under three different initial error states, the proposed controller drives the errors to zero across all cases. Through the aforementioned results, it is demonstrated that under arbitrary initial states NFTSMC can effectively control the space robot system to achieve successful trajectory tracking.

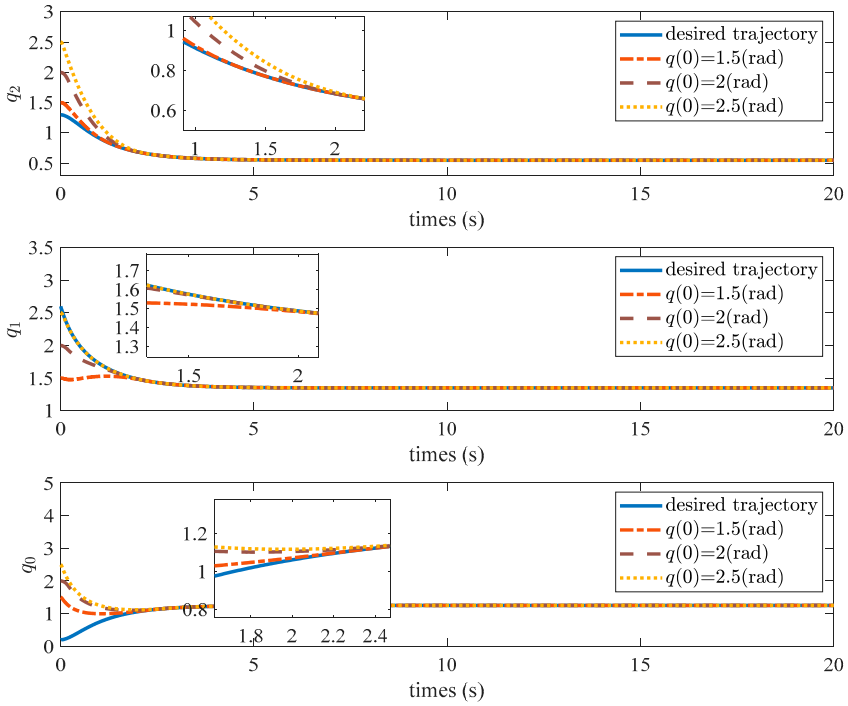


Figure 7. Trajectory tracking under different initial states.

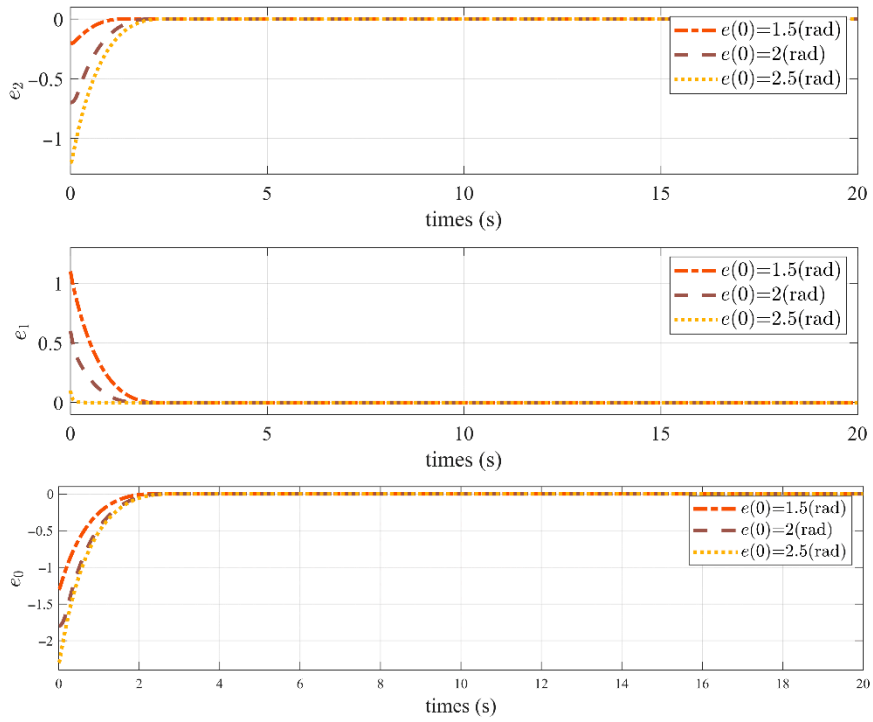


Figure 8. Trajectory tracking errors.

5.3. Case 3

Space robots operating in space are frequently subjected to disturbances from the solar wind, which cause changes to the system's inertial parameters. This case there-

fore considers model uncertainties in Equation (45). Leveraging the superior nonlinear approximation capability of neural networks, this paper employs a wavelet neural network to estimate model uncertainties. The detailed simulation processes are depicted in Figures 9–13. Figures 9 and 10 show the convergence performance of controller under lumped disturbances. The corresponding control input torques are presented in Figure 11. Furthermore, Figures 12 and 13 illustrate the adaptive processes of the neural network weights and the compensation term parameters, respectively.

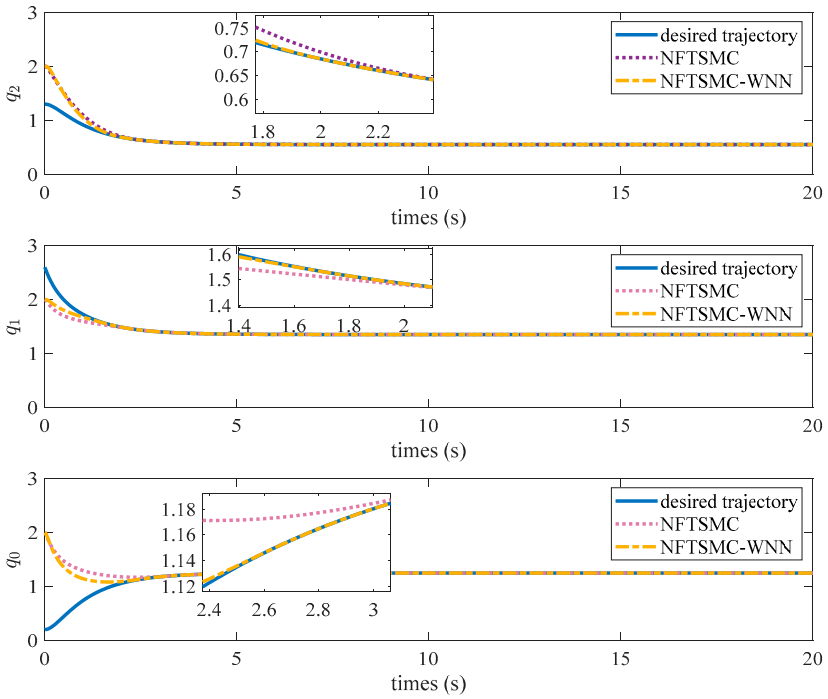


Figure 9. Trajectory tracking.

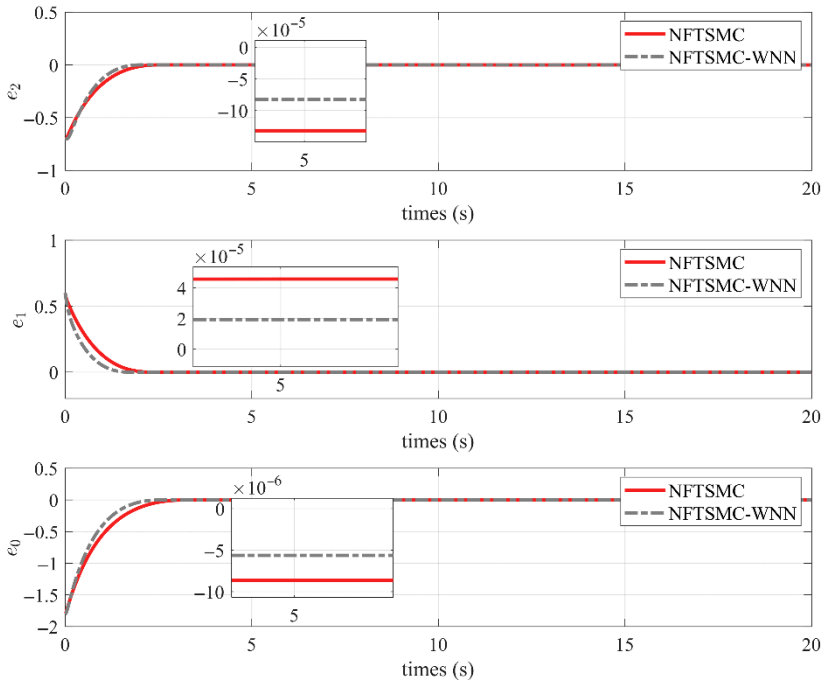


Figure 10. Trajectory tracking errors.

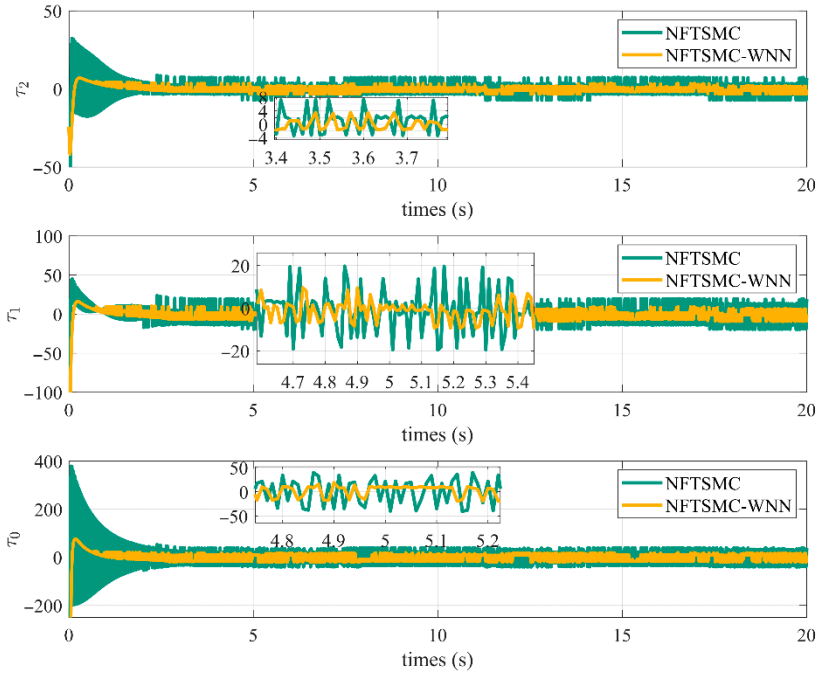


Figure 11. Input torques.

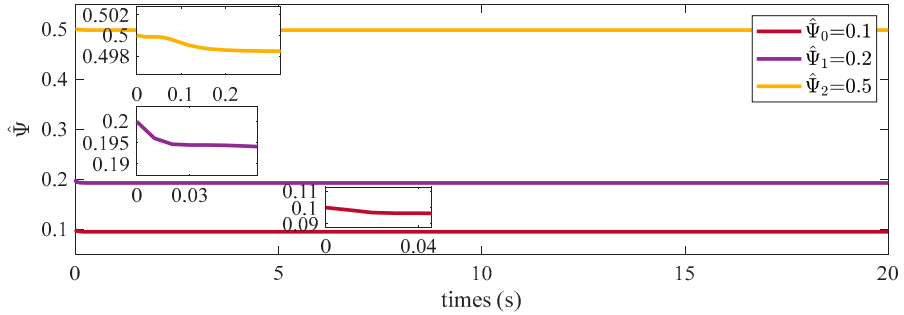


Figure 12. The adaptive value of $\hat{\psi}$.

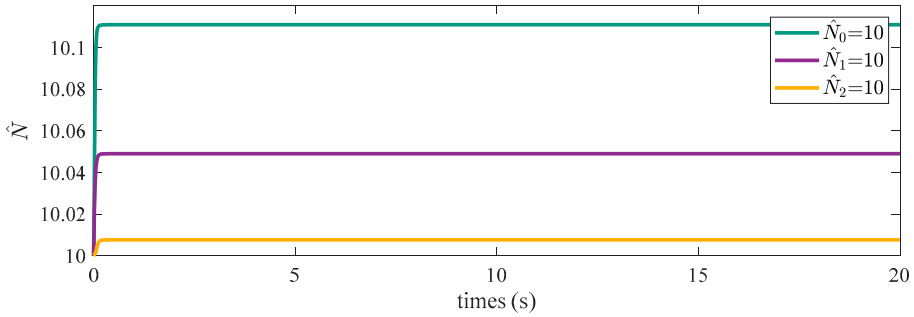


Figure 13. The adaptive value of $\hat{N}$.

Considering the existence of lumped disturbances, the tracking performance of the controllers under such lumped disturbances is presented in Figures 9 and 10. It is observed that Figure 9 presents the trajectory tracking of NFTSMC and NFTSMC-WNN under the same initial state. Notably, compared with method using NFTSMC, the proposed NFTSMC-WNN achieves faster smoother trajectory tracking. Its convergence times are 1.92 s, 1.59 s, and 2.54 s for the NFTSMC-WNN method while they are 2.36 s, 2.12 s, and 3.12 s for the NFTSMC method. Benefiting from the wavelet neural network, the NFTSMC-WNN converges faster than the NFTSMC, with an improvement of approximately 0.5 s.

The comparison results in Table 4 show that the error convergence rate of the control strategy proposed in this paper is significantly better than that of the pure NFTSMC algorithm, with an overall improvement in convergence performance of up to 20.74%. Although the pure NFTSMC algorithm resolves the singularity issues of traditional sliding mode control, its convergence rate and robustness remain limited when faced with system uncertainties and external disturbances. In this paper, we introduce a wavelet neural network (WNN) based on the NFTSMC. By using the WNN to perform online approximation and compensation of the system's lumped uncertainties, we effectively accelerate the error convergence rate of the system and further enhance the dynamic response performance and disturbance rejection capability of the control strategy.

Table 4. Controller performance comparison.

Joint	Controller	Convergence Time (s)	Improvement (%)	Overall Improvements (%)
q_0	Proposed NFTSMC	1.92 2.36	18.64	20.74
q_1	Proposed NFTSMC	1.59 2.12	25.00	
q_2	Proposed NFTSMC	2.54 3.12	18.59	

Figure 10 presents a comparison of the trajectory tracking errors between the NFTSMC and NFTSMC-WNN methods. It can be seen that WNN effectively estimates model uncertainty, with average tracking error accuracy under the NFTSMC-WNN method reaching 10^{-5} from 5 s~20 s and the average tracking errors of NFTSMC reaching 10^{-4}. These findings confirm the effectiveness of the WNN in estimating model uncertainties.

Figure 11 presents a comparison of the input torques between the NFTSMC method and the proposed NFTSMC–WNN method. Over the time interval from 5 s to 20 s, the average input torques of NFTSMC method are 5 N·m, 20 N·m, 40 N·m, while those for the NFTSMC-WNN method are 3 N·m, 8 N·m, 10 N·m. These results indicate that, compared to the NFTSMC method, the NFTSMC-WNN method generates smaller control torques and achieves superior performance.

Figure 12 shows the online estimation process for the WNN weights. It can be seen that the weight parameters converge at 0.2 s and then rapidly stabilize at steady-state values. Figure 13 shows the adaptive process of the compensation term parameter N, which effectively converges to a stable value over time. Case 3 analyzes a space robot with model uncertainties and demonstrates the superiority of the proposed NFTSMC-WNN strategy through Figures 9–13, which utilize wavelet neural networks for the online estimation of detailed uncertainties. The simulation results demonstrate the feasibility of the NFTSMC-WNN strategy and validate its potential application to space robot systems.

5.4. Case 4

In Case 4, to demonstrate the capability of the WNN within the proposed NFTSMC-WNN strategy for online uncertainty estimation, a comparative study is conducted with RBF neural network employed in the reference [35]. The detailed parameter configurations for the WNN and RBFNN are listed in Table 5, and Figures 14–16 show the simulation results.

Table 5. Detailed configuration and hyperparameter settings for WNN and RBFNN controllers.

Feature	WNN	RBFNN
Neuron	27	27
Activation Function	Mexican Hat	Radial Basis Function
Learning Rate	0.01	0.01
Initialization	$[0.1\ 0.2\ 0.5]^{T}$	$[0.1\ 0.2\ 0.5]^{T}$
Training Procedure	Input Layer, Hidden Layer, Output Layer	Input Layer, Hidden Layer, Output Layer
Network Structure	Feedforward Neural Network	Feedforward Neural Network

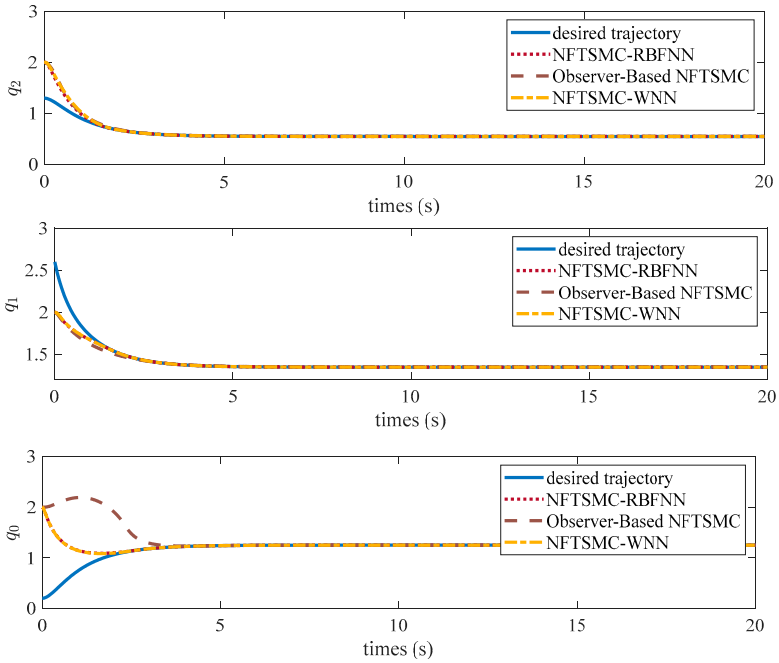


Figure 14. Trajectory tracking.

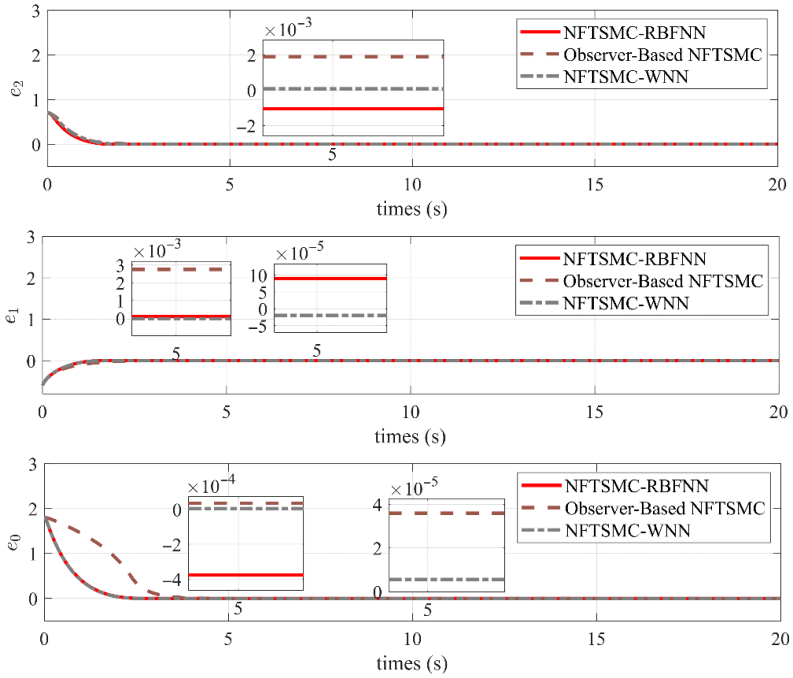


Figure 15. Trajectory tracking errors.

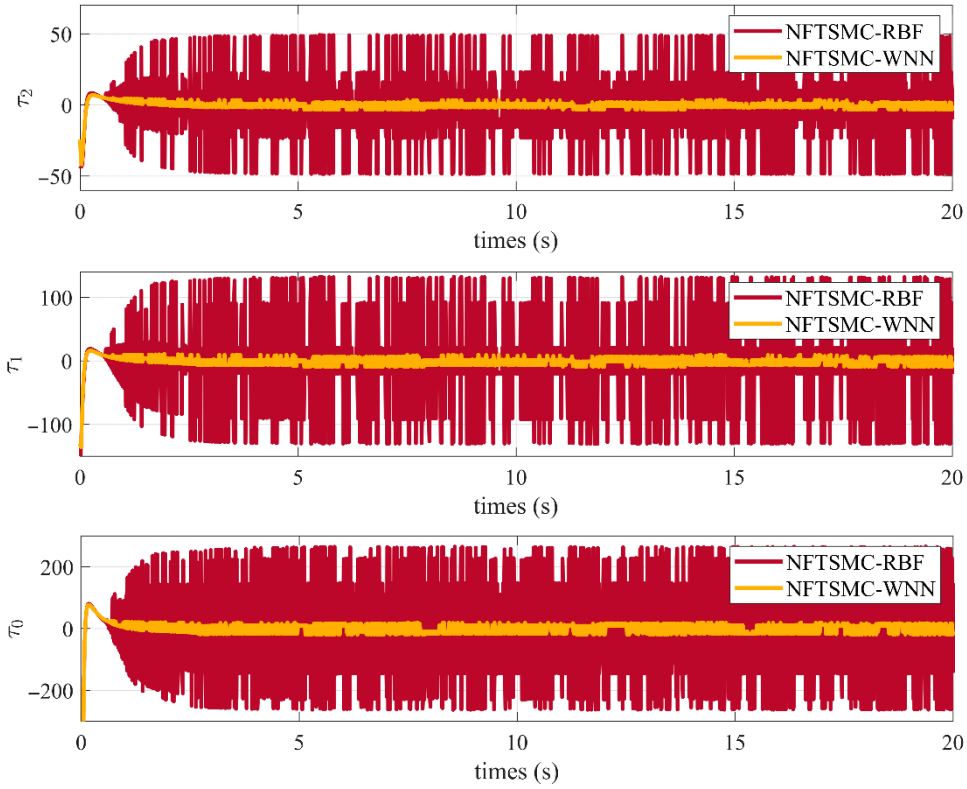


Figure 16. Input torques.

As shown in Table 5, the number of neurons and the selection of hyperparameters for the RBFNN and WNN were kept consistent to ensure a fair comparison of the control algorithms. The wavelet neural network was constructed based on the topology of an error backpropagation neural network. While structurally similar to neural networks, the distinctive feature of the wavelet neural network is its use of wavelet basis functions as transfer functions for hidden layer nodes. The Mexican hat function was selected due to its widespread use in transient detection and its high sensitivity to disturbance variations.

As shown in Figure 14, both RBFNN and WNN demonstrate comparable capabilities in estimating uncertainties and exhibit similar convergence rates, both converging at 2 s. This estimated ability is derived from their respective network structures. Although Figure 14 indicates that the WNN and RBFNN possess comparable compensation capabilities; Figure 15 compares their trajectory tracking error, revealing that under identical network structures, the WNN method achieves an accuracy of 10^{-5}, while the RBFNN method only reaches 10^{-4}. This demonstrates that WNN significantly outperforms RBFNN, exhibiting superior online uncertainty estimation. In Figures 14 and 15, by employing the disturbance observer to estimate the lumped uncertainty, it can be observed that its performance is inferior to that of the proposed wavelet neural network (WNN) in terms of convergence speed and tracking accuracy. The inclusion of NFTSMC based on the disturbance observer further highlights the practical applicability and superior operability of the proposed control strategy.

Table 6 compares the trajectory tracking error convergence performance of the proposed control strategy with that of the NFTSMC-RBF algorithm. The results show that, compared to the benchmark algorithm, the proposed strategy achieves shorter error convergence times at all robot joints, and the overall convergence speed is significantly improved. This validates that the proposed control strategy offers superior dynamic response performance and is better suited to meet the real-time control requirements of spatial robot grasping tasks.

Table 6. Comparison of convergence time between NFTSMC-RBF and the proposed control.

Joint	Controller	Convergence Time (s)	Improvement (%)	Overall Improvements (%)
q_0	Proposed	2.75	1.08	1.92
	NFTSMC-RBF	2.78		
q_1	Proposed	1.74	1.13	
	NFTSMC-RBF	1.76		
q_2	Proposed	1.9	3.55	
	NFTSMC-RBF	1.97		

Figure 16 compares the input torques of NFTSMC-RBFNN and NFTSMC-WNN. It can be observed that the input torque under RBFNN is 50 N·m, 120 N·m, and 220 N·m over the course of 2 s to 20 s., whereas under WNN, it is 3 N·m, 8 N·m, and 10 N·m over the same period. As shown in Figure 16, the input torque of NFTSMC-WNN is significantly smaller than that of NFTSMC-RBFNN, highlighting WNN's superior capability in handling uncertainty compared to RBFNN. From the foregoing discussions, these findings provide strong evidence for the feasibility of NFTSMC-WNN strategy.

The simulation comparisons in Cases 3 and 4 have demonstrated the performance advantages of the proposed control algorithm over NFTSMC and NFTSMC-RBF. To provide a visual quantification of these advantages, Table 7 summarizes the tracking performance of each algorithm, while Table 8 summarizes the energy consumption and control smoothness metrics.

Table 7. Tracking performance comparison.

Joint	Controller	Mean Error (rad)	RMSE (rad)	IAE (rad)	ITAE (rad)
q_0	Proposed	8.2062×10^{-7}	1.8188×10^{-5}	1.5479×10^{-4}	7.7746×10^{-4}
	NFTSMC	2.8777×10^{-6}	3.0297×10^{-5}	2.6152×10^{-4}	1.3019×10^{-3}
	NFTSMC-RBF	-3.6183×10^{-6}	2.0336×10^{-4}	1.6964×10^{-3}	8.4812×10^{-3}
q_1	Proposed	1.0888×10^{-5}	1.8890×10^{-5}	1.5757×10^{-4}	8.0826×10^{-4}
	NFTSMC	2.2947×10^{-6}	3.1501×10^{-5}	2.6901×10^{-4}	1.3594×10^{-3}
	NFTSMC-RBF	-7.8962×10^{-6}	2.2915×10^{-4}	1.8708×10^{-3}	-9.4175×10^{-3}
q_2	Proposed	-6.0091×10^{-5}	1.4855×10^{-4}	1.3584×10^{-3}	7.2543×10^{-3}
	NFTSMC	-1.3698×10^{-4}	2.2757×10^{-4}	1.8349×10^{-3}	1.0077×10^{-2}
	NFTSMC-RBF	1.1156×10^{-5}	3.3738×10^{-4}	2.8204×10^{-3}	-2.5112×10^{-2}

Table 8. Energy consumption and control smoothness.

Joint	Controller	Energy Consumption (J)	Control Smoothness (J^2/s)
q_0	Proposed	0.1810	3.16107×10^7
	NFTSMC	18.16	2.3633×10^8
	RBF	4.1797	2.58678×10^9
q_1	Proposed	2.5895	3.04162×10^6
	NFTSMC	6.2756	3.15032×10^7
	RBF	2.4821	3.96135×10^8
q_2	Proposed	4.2739	3.16409×10^5
	NFTSMC	6.6744	1.82690×10^6
	RBF	3.3465	4.89273×10^7

Table 7 presents the trajectory tracking performance comparison results, which verify that the proposed control algorithm significantly outperforms the two contrast algorithms.

Compared with the conventional NFTSMC algorithm, the mean tracking error, root mean square error (RMSE), integral absolute error (IAE) and integral time-weighted absolute error (ITAE) of the proposed algorithm are reduced by 63.29%, 35.85%, 29.37% and 93.06%, respectively; compared with the NFTSMC-RBF algorithm, the above four metrics are reduced by 87.75%, 81.66%, 80.25% and 73.54%, respectively. These results fully validate the superior performance of the proposed algorithm in trajectory tracking accuracy and error convergence.

The energy consumption is quantified by the integral of the control torque $E = \int \sum_{0}^{2} \boldsymbol{\tau}_i \cdot \dot{\boldsymbol{q}}_i dt$, which reflects the physical effort of the actuators. The smoothness is assessed by the integral of the squared torque derivative $S = \int \sum_{0}^{2} \left(\frac{d\boldsymbol{\tau}_i}{dt} \right)^2 dt$, which penalizes abrupt changes in the control input and ensures a gentler motion.

Table 8 presents the quantitative comparison results, confirming that the proposed control strategy demonstrates significant advantages in both energy utilization efficiency and control smoothness. Compared with the NFTSMC algorithm, the proposed strategy improves energy utilization efficiency by 77.36% and control smoothness by 87.03%. Compared with the NFTSMC-RBF algorithm, improvements of 29.61% and 98.85% are achieved in energy utilization efficiency and control smoothness, respectively.

6. Conclusions

This paper aims to address the trajectory tracking challenge for space robots operating under lumped uncertainties by proposing a novel wavelet neural network-based NFTSMC methodology. This strategy combines a new NFTSM surface with a WNN. The adaptive wavelet neural network NFTSMC strategy offers two key advantages. First, it guarantees the finite-time convergence of the space robot system. Secondly, it possesses sliding mode disturbance rejection capabilities and is robust against external disturbances. Thirdly, it can effectively estimate and compensate for uncertainties in the space robot. The feasibility of the NFTSMC-WNN method was subsequently demonstrated using Lyapunov stability theory. Numerical simulations showed that the NFTSMC-WNN method reduced system convergence time by 28.57% and improved trajectory tracking accuracy. Together, these findings confirm the technical feasibility of the proposed strategy. Furthermore, future work will explore lightweight WNNs to advance the deployment of on-orbit servicing for space robots.

Author Contributions: Conceptualization, H.A.; methodology, H.A. and A.Z.; software, Y.Z. and J.M.; investigation, A.Z. and H.A.; writing—original draft preparation, J.M. and Y.Z.; writing—review and editing, A.Z. and H.A.; supervision, H.A. and F.X.; funding acquisition, H.A. and X.F. All authors have read and agreed to the published version of the manuscript.

Funding: Jiangxi Provincial Natural Science Foundation under Grants 20232BAB212030, 20242BAB25258 and 20252BAC200187, the Jiangxi Provincial Key Laboratory of Particle Technology under Grants 20242BCC32119, and the Doctor research start-up fund of Jiangxi University of Science and Technology (205200100687).

Data Availability Statement: Data supporting results are included in the manuscript.

Conflicts of Interest: The authors declare no conflicts of interest.

References

1. Zhang, X.; Liu, J.; Tong, Y.; Liu, Y.; Ju, Z. Attitude decoupling control of semifloating space robots using time-delay estimation and supertwisting control. *IEEE Trans. Aerosp. Electron. Syst.* **2021**, *57*, 4280–4295. [CrossRef]
2. Zou, W.; Shi, T.; Guo, J.; Xiang, Z. A novel adaptive fuzzy control scheme for a class of nonlinear planar systems under state constraints. *IEEE Trans. Circuits Syst. II Express Briefs* **2023**, *71*, 827–831. [CrossRef]

3. Wang, C.; Guo, Q.; Wang, J.; Liu, Z.; Chen, C.L.P. Fixed-time fuzzy control for uncertain nonlinear systems with prescribed performance and event-triggered communication. *IEEE Trans. Circuits Syst. I Regul. Pap.* **2024**, *71*, 2362–2371. [CrossRef]
4. Zhao, J.; Lv, Y.; Zeng, Q.; Wan, L. Online policy learning-based output-feedback optimal control of continuous-time systems. *IEEE Trans. Circuits Syst. II Express Briefs* **2022**, *71*, 652–656. [CrossRef]
5. Yang, W.; Lam, H.K.; Cui, G.; Yu, J. Command filter-based adaptive optimal control of uncertain nonlinear systems with quantized input. *IEEE Trans. Fuzzy Syst.* **2023**, *32*, 343–348. [CrossRef]
6. Ge, L.; Guo, J.; Mao, S.; Xiao, D.; Zhao, D.; Song, S.; De Doncker, R.W. A composite model predictive control method of SRMs with PWM-based signal for torque ripple suppression. *IEEE Trans. Transp. Electrif.* **2023**, *10*, 2469–2478. [CrossRef]
7. Zhang, X.; Liu, Z.; Zhang, P.; Zhang, Y. Model predictive current control for PMSM drives based on nonparametric prediction model. *IEEE Trans. Transp. Electrif.* **2023**, *10*, 711–719. [CrossRef]
8. Pan, J.; Shao, B.; Xiong, J.; Zhang, Q. Attitude control of quadrotor UAVs based on adaptive sliding mode. *Int. J. Control Autom. Syst.* **2023**, *21*, 2698–2707. [CrossRef]
9. Yan, Y.; Yu, S.; Gao, X.; Wu, D.; Li, T. Continuous and periodic event-triggered sliding-mode control for path following of underactuated surface vehicles. *IEEE Trans. Cybern.* **2023**, *54*, 449–461. [CrossRef]
10. Yang, J.; Li, S.; Yu, X. Sliding-mode control for systems with mismatched uncertainties via a disturbance observer. *IEEE Trans. Ind. Electron.* **2012**, *60*, 160–169. [CrossRef]
11. Yao, Q.; Li, Q.; Xi, Y.; Jahanshahi, H. Extended state filter-based velocity-free finite-time attitude control of spacecraft. *Int. J. Robust Nonlinear Control* **2024**, *34*, 5540–5552. [CrossRef]
12. Fu, X.; Ai, H.; Chen, L. Integrated sliding mode control with input restriction, output feedback and repetitive learning for space robot with flexible-base, flexible-link and flexible-joint. *Robotica* **2023**, *41*, 370–391. [CrossRef]
13. Hou, H.; Yu, X.; Xu, L.; Rsetam, K.; Cao, Z. Finite-time continuous terminal sliding mode control of servo motor systems. *IEEE Trans. Ind. Electron.* **2019**, *67*, 5647–5656. [CrossRef]
14. Xiong, J.J.; Zhang, G.B. Global fast dynamic terminal sliding mode control for a quadrotor UAV. *ISA Trans.* **2017**, *66*, 233–240. [CrossRef] [PubMed]
15. Qin, C.; Zhang, Z.; Fang, Q. Adaptive backstepping fast terminal sliding mode control with estimated inverse hysteresis compensation for piezoelectric positioning stages. *IEEE Trans. Circuits Syst. II Express Briefs* **2023**, *71*, 1186–1190. [CrossRef]
16. Yang, Q.; Ma, X.; Wang, W.; Peng, D. Adaptive non-singular fast terminal sliding mode trajectory tracking control for robot manipulators. *Electronics* **2022**, *11*, 3672. [CrossRef]
17. Chen, Y.; Li, F.; Zhang, L. Fixed-time nonsingular terminal sliding mode control for trajectory tracking of uncertain robot manipulators. *Trans. Inst. Meas. Control* **2024**, *46*, 2414–2425. [CrossRef]
18. Guo, L.; Guan, L.; Jiang, H.; Ma, H.; Xu, L.; Wang, X. Nonsingular terminal sliding mode controller-based path tracking control for autonomous vehicles considering multiple-uncertainties disturbances. *Proc. Inst. Mech. Eng. Part D J. Automob. Eng.* **2025**, *239*, 4857–4880. [CrossRef]
19. Li, Y.; Zhang, Z. High-Order Nonsingular Fast Integral Terminal Sliding Mode Control with Perturbation Estimation for a Class of Nonlinear Hysteresis Systems. *IEEE Trans. Ind. Electron.* **2024**, *72*, 2045–2055. [CrossRef]
20. Xu, D.; Ding, B.; Jiang, B.; Yang, W.; Shi, P. Nonsingular fast terminal sliding mode control for permanent magnet linear synchronous motor via high-order super-twisting observer. *IEEE/ASME Trans. Mechatron.* **2021**, *27*, 1651–1659. [CrossRef]
21. Hong, M.; Gu, X.; Liu, L.; Guo, Y. Finite time extended state observer based nonsingular fast terminal sliding mode control of flexible-joint manipulators with unknown disturbance. *J. Frankl. Inst.* **2023**, *360*, 18–37. [CrossRef]
22. Wang, F.; Ma, Z.; Gao, H.; Zhou, C.; Hua, C. Disturbance observer-based nonsingular fast terminal sliding mode fault tolerant control of a quadrotor UAV with external disturbances and actuator faults. *Int. J. Control Autom. Syst.* **2022**, *20*, 1122–1130. [CrossRef]
23. Shang, D.; Li, X.; Yin, M.; Li, F. Dynamic modeling and RBF neural network compensation control for space flexible manipulator with an underactuated hand. *Chin. J. Aeronaut.* **2024**, *37*, 417–439. [CrossRef]
24. Yu, L.; Qiu, Z.; Zhang, X. Radial basis function neural network vibration control of a flexible planar parallel manipulator based on acceleration feedback. *J. Vib. Control* **2022**, *28*, 351–363. [CrossRef]
25. Zhang, H.; Yu, J.; Shi, P.; Hu, S.; Zhao, L. Adaptive continuous fractional-order nonsingular terminal sliding mode control based on neural network for PMLM system with actuator saturation. *Neurocomputing* **2025**, *646*, 130468. [CrossRef]
26. Luo, G.; Chen, B. Applying adaptive wavelet neural network and sliding mode control for tracking control of MEMS gyroscope. *Electron. Lett.* **2025**, *61*, e70187. [CrossRef]
27. Liu, W.; Liu, L.; Zhang, D.; Cheng, J. Nonsingular fast terminal sliding mode control of uncertain robotic manipulator system based on adaptive fuzzy wavelet neural network. *Int. J. Fuzzy Syst.* **2025**, *27*, 898–911. [CrossRef]
28. Liu, Z.; Gao, H.; Yu, X.; Lin, W.; Qiu, J.; Rodríguez-Andina, J.J.; Qu, D. B-spline wavelet neural-network-based adaptive control for linear-motor-driven systems via a novel gradient descent algorithm. *IEEE Trans. Ind. Electron.* **2023**, *71*, 1896–1905. [CrossRef]

29. Tlijani, H.; Jouila, A.; Nouri, K. Wavelet neural network sliding mode control of two rigid joint robot manipulator. *Adv. Mech. Eng.* **2022**, *14*, 16878132221119886. [CrossRef]
30. Chen, S.H.; Mao, W.L.; Lu, W.X. Application of the adaptive fuzzy wavelet neural network for two-axis trajectory control. *IET Control Theory Appl.* **2022**, *16*, 1015–1031. [CrossRef]
31. Zhu, A.; Ai, H.; Chen, L. FSTSMC Compliance Control for Dual-Arm Space Robot with SDBD Capture Satellite Operation. *J. Comput. Nonlinear Dyn.* **2023**, *18*, 061006. [CrossRef]
32. Jeong, S.; Chwa, D. Sliding-mode-disturbance-observer-based robust tracking control for omnidirectional mobile robots with kinematic and dynamic uncertainties. *IEEE/ASME Trans. Mechatron.* **2020**, *26*, 741–752. [CrossRef]
33. Yu, J.; Shi, P.; Zhao, L. Finite-time command filtered backstepping control for a class of nonlinear systems. *Automatica* **2018**, *92*, 173–180. [CrossRef]
34. Feng, Y.; Yu, X.; Han, F. On nonsingular terminal sliding-mode control of nonlinear systems. *Automatica* **2013**, *49*, 1715–1722. [CrossRef]
35. Wei-Dong, D.; Wen-Ping, J. Two-degree-of-freedom robotic arm based on RBF neural network approximation control method research. In *Proceedings of the 2022 7th International Conference on Intelligent Informatics and Biomedical Science (ICIIBMS), Nara, Japan, 24–26 November 2022*; IEEE: Piscataway, NJ, USA, 2022; Volume 7, pp. 150–154. [CrossRef]

Disclaimer/Publisher's Note: The statements, opinions and data contained in all publications are solely those of the individual author(s) and contributor(s) and not of MDPI and/or the editor(s). MDPI and/or the editor(s) disclaim responsibility for any injury to people or property resulting from any ideas, methods, instructions or products referred to in the content.